



Radio Spectra and Sizes of Atacama Large Millimeter/submillimeter Array-identified Submillimeter Galaxies: Evidence of Age-related Spectral Curvature and Cosmic-Ray Diffusion?

A. P. Thomson^{1,2}, Ian Smail², A. M. Swinbank², J. M. Simpson^{3,19}, V. Arumugam⁴, S. Stach², E. J. Murphy⁵, W. Rujopakarn^{6,7,8}, O. Almaini⁹, F. An², A. W. Blain¹⁰, C. C. Chen⁴, E. A. Cooke², U. Dudzevičiūtė², A. C. Edge², D. Farrah^{11,12}, B. Gullberg², W. Hartley¹³, E. Ibar¹⁴, D. Maltby⁹, M. J. Michałowski¹⁵, C. Simpson¹⁶, P. van der Werf¹⁷, and J. L. Wardlow¹⁸

¹ Jodrell Bank Centre for Astrophysics, The University of Manchester, Oxford Road, Manchester M13 9PL, UK; alasdair.thomson@manchester.ac.uk

² Centre for Extragalactic Astronomy, Department of Physics, Durham University, South Road, Durham DH1 3LE, UK

³ Academia Sinica Institute of Astronomy and Astrophysics, No. 1, Section 4, Roosevelt Road, Taipei 10617, Taiwan

⁴ European Southern Observatory, Karl Schwarzschild Strasse 2, Garching, Germany

⁵ National Radio Astronomy Observatory, 520 Edgemont Road, Charlottesville, VA 22903, USA

⁶ Department of Physics, Faculty of Science, Chulalongkorn University, 254 Phayathai Road, Pathumwan, Bangkok 10330, Thailand

⁷ National Astronomical Research Institute of Thailand (Public Organization), Don Kaeo, Mae Rim, Chiang Mai 50180, Thailand

⁸ Kavli Institute for the Physics and Mathematics of the Universe (WPI), The University of Tokyo Institutes for Advanced Study, The University of Tokyo, Kashiwa, Chiba 277-8583, Japan

⁹ School of Physics and Astronomy, University of Nottingham, University Park, Nottingham NG7 2RD, UK

¹⁰ Astronomical Observatory Institute, Faculty of Physics, Adam Mickiewicz University, ul. Słoneczna 36, 60-286 Poznań, Poland

¹¹ Department of Physics and Astronomy, University of Hawaii, 2505 Correa Road, Honolulu, HI 96822, USA

¹² Institute for Astronomy, 2680 Woodlawn Drive, University of Hawaii, Honolulu, HI 96822, USA

¹³ Department of Physics and Astronomy, University College London, 3rd Floor, 132 Hampstead Road, London NW1 2PS, UK

¹⁴ Instituto de Física y Astronomía, Universidad de Valparaíso, Avda. Gran Bretaña 1111, Valparaíso, Chile

¹⁵ University of Leicester, Physics & Astronomy, University Road, Leicester LE1 7RH, UK

¹⁶ Gemini Observatory, Northern Operations Center, 670 North A'ohōku Place, Hilo, HI 96720-2700, USA

¹⁷ Leiden Observatory, Leiden University, P.O. Box 9513, NL-2300 RA Leiden, The Netherlands

¹⁸ Department of Physics, Lancaster University, Lancaster LA1 4 YB, UK

Received 2017 October 9; revised 2019 July 12; accepted 2019 July 15; published 2019 October 4

Abstract

We analyze the multifrequency radio spectral properties of 41 6 GHz-detected Atacama Large Millimeter/submillimeter Array (ALMA)-identified, submillimeter galaxies (SMGs), observed at 610 MHz, 1.4 GHz, and 6 GHz with the Giant Metrewave Radio Telescope and the Very Large Array. Combining high-resolution ($\sim 0''.5$) 6 GHz radio and ALMA 870 μm imaging (tracing rest frame ~ 20 GHz, and ~ 250 μm dust continuum), we study the far-infrared/radio correlation via the logarithmic flux ratio q_{IR} , measuring $\langle q_{\text{IR}} \rangle = 2.20 \pm 0.06$ for our sample. We show that the high-frequency radio sizes of SMGs are $\sim 1.9 \pm 0.4 \times (\sim 2\text{--}3 \text{ kpc})$ larger than those of the cool dust emission, and find evidence for a subset of our sources being extended on ~ 10 kpc scales at 1.4 GHz. By combining radio flux densities measured at three frequencies, we can move beyond simple linear fits to the radio spectra of high-redshift star-forming galaxies, and search for spectral curvature, which has been observed in local starburst galaxies. At least a quarter (10/41) of our sample shows evidence of a spectral break, with a median $\langle \alpha_{610 \text{ GHz}}^{1.4 \text{ GHz}} \rangle = -0.60 \pm 0.06$, but $\langle \alpha_{1.4 \text{ GHz}}^{6 \text{ GHz}} \rangle = -1.06 \pm 0.04$ —a high-frequency flux deficit relative to simple extrapolations from the low-frequency data. We explore this result within this subset of sources in the context of age-related synchrotron losses, showing that a combination of weak magnetic fields ($B \sim 35 \mu\text{G}$) and young ages ($t_{\text{SB}} \sim 40\text{--}80 \text{ Myr}$) for the central starburst can reproduce the observed spectral break. Assuming these represent evolved (but ongoing) starbursts, and we are observing these systems roughly halfway through their current episode of star formation, this implies starburst durations of $\lesssim 100 \text{ Myr}$, in reasonable agreement with estimates derived via gas depletion timescales.

Key words: cosmic rays – galaxies: evolution – galaxies: high-redshift – galaxies: starburst – radio continuum: galaxies – submillimeter: galaxies

1. Introduction

Galaxies selected in the observed frame $\sim 850 \mu\text{m}$ window (submillimeter-selected galaxies, hereafter SMGs) represent a class of extreme star-forming galaxies at cosmological distances. Their rest-frame spectral energy distributions (SEDs) peak in the far-infrared (far-IR), due to the reprocessing of optical/ultraviolet starlight by large column densities of interstellar dust. The far-IR luminosities of SMGs ($L_{\text{IR}} \geq 10^{12} L_{\odot}$) are similar to those of local ultraluminous

infrared galaxies (ULIRGs), and imply large dust masses and high star formation rates (SFRs) ($M_{\text{dust}} \gtrsim 5 \times 10^8 M_{\odot}$, $\text{SFR} \geq 200 M_{\odot} \text{ yr}^{-1}$, e.g., da Cunha et al. 2015), while their redshift distribution peaks at $z \sim 2\text{--}3$ (albeit with a significant tail extending to $z > 4$, e.g., Chapman et al. 2005; Simpson et al. 2014; Brisbin et al. 2017; Danielson et al. 2017). At this epoch, SMGs are $\sim 1000\times$ more numerous than their low-redshift ULIRG counterparts, and are thought to account for $\sim 20\%\text{--}40\%$ of cosmic star formation (e.g., Hughes et al. 1998; Yun et al. 2012; Swinbank et al. 2014). The clustering (e.g., Hickox et al. 2012; Wilkinson et al. 2017), SFRs, and large gas

¹⁹ EACOA fellow.

reservoirs (e.g., Bothwell et al. 2013) of SMGs have led to suggestions that they represent a crucial phase in the assembly of local, massive “red and dead” elliptical galaxies (e.g., Simpson et al. 2014; Toft et al. 2014; Hodge et al. 2016).

While much has been learned about the SMG population since the first submillimeter bolometer observations at the end of the last century (e.g., Smail et al. 1997; Hughes et al. 1998), a long-standing problem lay in the difficulty of identifying multiwavelength counterparts to the sources detected in low-resolution single-dish submillimeter maps. Exploitation of the relationship between the far-IR and radio emission in star-forming galaxies, allied with the subarcsecond resolution of radio interferometers has served as a useful route to identifying SMG counterparts (e.g., Ivison et al. 1998, 2002), but recent work with the Atacama Large Millimeter Array (ALMA)—which allows high-resolution submillimeter images to be made—circumvents the need to probabilistically associate the submillimeter flux seen in single-dish studies with emission in other wave bands (e.g., Hodge et al. 2013; Stach et al. 2019).

Nevertheless, deep radio observations continue to provide invaluable insight into the nature of SMGs, with lower frequency ($\nu_{\text{rest}} \lesssim 10$ GHz) observations revealing steep-spectrum ($\alpha \sim -0.8$, where $S_\nu \propto \nu^\alpha$) synchrotron emission (which in star-forming galaxies is produced predominantly by supernovae (SNe), and in galaxies hosting an active galactic nucleus (AGN) provides a window into the central black hole itself), and higher frequency ($\nu_{\text{rest}} \gtrsim 10$ GHz) observations tracing flatter spectrum ($\alpha \sim -0.1$) thermal free-free emission, which is believed to arise from the scattering of free-electrons in the H II regions around young, massive star clusters (e.g., Condon 1992). The lack of dust obscuration in the radio bands ensures that radio observations are as sensitive to dust-obscured star formation (which can also be seen in the far-IR, but generally not in the optical/ultraviolet) as they are to unobscured star formation (which may be seen in the optical/ultraviolet, but not in the far-IR), thus making deep radio imaging an important dust-unbiased tracer of star formation (e.g., Ivison et al. 2007). However, the strong positive k -correction in the radio bands makes it increasingly more difficult to detect star formation in galaxies at $z \gtrsim 3$, at which a significant fraction of the SMG population is believed to lie. Moreover, the dual origin of radio emission in galaxies (i.e., star formation and AGN activity) makes the interpretation of radio maps of high-redshift sources dependent on information from other wave bands.

On galaxy-integrated scales, the observed correlation between the far-IR and radio luminosities of star formation-dominated galaxies (the far-IR/radio correlation; Helou et al. 1985) provides one route toward discriminating dusty starbursts from Compton-thick AGN (e.g., Del Moro et al. 2013). This correlation spans several orders of magnitude in spatial scale, luminosity, gas surface density, and photon/magnetic field density, and owes its existence to the link between both IR and radio emission and the formation and destruction of massive stars. In the simplest “calorimetry” models (e.g., Lisenfeld et al. 1996), the optical/ultraviolet light produced by young, massive stars is absorbed by dust and re-radiated in the far-IR; at the end of their (short) lives, the SNe produced by these same stars inject cosmic-ray electrons (CREs) into the interstellar medium (ISM), whose eventual energy loss via interaction with the magnetic field of the host galaxy produces synchrotron radio emission. Thus, the far-IR/radio correlation emerges for star-forming systems on timescales longer than the lifetimes of typical OB stars ($\gtrsim 10$ Myr). Extensive work in

samples of higher redshift galaxies has shown that this correlation broadly holds at out to at least $z \sim 4$ (Garrett 2002; Murphy 2009; Bourne et al. 2011), with evidence for a modest evolution with redshift ($q_{\text{IR}} \propto (1+z)^{-n}$, with $n \lesssim 0.2$; Ivison et al. 2010; Magnelli et al. 2015; Calistro Rivera et al. 2017; Delhaize et al. 2017).

However at high redshift, accurate measurements of the radio luminosity densities of galaxies (by convention, measured at rest frame 1.4 GHz), depend on a k -correction of the observed-frame flux densities to the rest frame, and the magnitude of this k -correction is sensitive to the radio spectral index. In a resolution-matched study of 57 Lockman Hole SMGs observed at 610 MHz and 1.4 GHz with the Giant Metrewave Radio Telescope (GMRT) and Karl G. Jansky Very Large Array (VLA), reaching 1σ sensitivities of 15 and $6 \mu\text{Jy beam}^{-1}$, respectively, Ibar et al. (2010) measured a median radio spectral index of $\alpha_{610 \text{ MHz}}^{1.4 \text{ GHz}} = -0.75 \pm 0.06$. Later, in a sample of 52 ALMA-identified SMGs from the Extended Chandra Deep Field South (ECDFS) field (the “ALESS” sample), Thomson et al. (2014) measured a median radio spectral index $\alpha_{610 \text{ MHz}}^{1.4 \text{ GHz}} = -0.79 \pm 0.06$. In both cases, the measured spectral indices were found to be consistent with synchrotron-dominated emission at low radio frequencies. However, some studies have found evidence of spectral flattening at low frequencies ($\alpha_{610 \text{ MHz}}^{1.4 \text{ GHz}} \gtrsim -0.5$) both in local ULIRGs (Smith et al. 1998) and in high-redshift SMGs (Hunt & Maiolino 2005), while others have found evidence of spectral steepening at higher frequencies ($\nu \gtrsim 10$ GHz; Galvin et al. 2018; Jiménez-Andrade et al. 2019), in good agreement with models in which the production of secondary electrons and positrons competes with (sometimes rapid) cooling of CREs due to bremsstrahlung, ionization, and inverse Compton processes, which suppresses high-frequency radio emission (Lacki & Thompson 2010; Basu et al. 2015). Together, these works suggest that the rest frame ~ 1 –30 GHz radio emission in at least some ULIRGs and SMGs is likely to be more complex than a simple sum of two power laws.

Observations of SMGs with single-dish submillimeter facilities and radio interferometers have shown that, in a galaxy-averaged sense, SMGs typically lie on/close to the local far-IR/radio correlation (e.g., Ivison et al. 2010; Thomson et al. 2014). Since far-IR and radio emission are both thought—in the absence of a strong AGN—to be produced by processes related to star formation, one might anticipate that this relation would hold in SMGs down to the scales probed by our radio and submillimeter observations ($\lesssim 5$ kpc), as in local dwarf galaxies (e.g., Schleicher & Beck 2016). However, direct comparison of the sizes of the far-IR and radio emission for the same sources has long proved challenging at high redshift, due to the scarcity of high-resolution, interferometric imaging in the far-IR bands to compare with the deep radio imaging by which counterparts to single-dish submillimeter sources were first identified. Only in the era of submillimeter interferometry ushered in by the Submillimeter Array (SMA) and ALMA has such a direct comparison between the rest-frame far-IR and radio morphologies of SMGs become possible.

In order to investigate the relationship between the radio and dust continuum emission in SMGs, we have conducted a pilot study of the radio spectral properties of submillimeter galaxies detected in the ALMA survey of the SCUBA-2 Cosmology Legacy Survey UK Infrared Telescope Infrared Deep Sky Survey (UKIDSS)/Ultra-Deep Survey (UDS) field (hereafter

AS2UDS; Stach et al. 2019). Using a series of sensitive ($\sigma_{6\text{ GHz}} \sim 2.7\ \mu\text{Jy beam}^{-1}$), targeted high-resolution ($\sim 0''.5$) C-band (6 GHz) observations obtained with the VLA in A-configuration along with an extremely deep ($\sigma_{6\text{ GHz}} \sim 0.7\ \mu\text{Jy beam}^{-1}$) two-pointing C-band mosaic made from archival data, we perform a direct comparison of the spatial extents, orientations, and morphologies of the radio and dust emission of our SMG targets. By exploiting sensitive VLA L-band (1.4 GHz) and GMRT 610 MHz imaging (Ibar 2009), we also gain new constraints on the radio spectral properties of our sources across two intervals in frequency, allowing our analysis to move beyond simple power-law characterizations of the radio spectral index, and to search for signs of spectral index curvature.

The remainder of this paper is structured as follows: in Section 2, we present our sample and observations, including a description of the preexisting ALMA 870 μm , VLA 1.4 GHz, and GMRT 610 MHz observations, as well as a description of the observing, data reduction, and imaging strategies used to produce our new VLA 6 GHz images. In Section 3, we present our results and analysis. We discuss our results in Section 4, in which we develop a model whereby both the curved radio spectra and the changes we observe in radio morphology as a function of frequency are explored within the context synchrotron spectral aging. In Section 5 we summarize and offer concluding remarks.

Throughout our manuscript we adopt a Λ -cold dark matter cosmology with $H_0 = 71\ \text{km s}^{-1}\text{Mpc}$, $\Omega_m = 0.27$ and $\Omega_\Lambda = 0.73$.

2. Observations and Data Reduction

2.1. SCUBA-2/ALMA 870 μm

The SMGs in our sample were selected from observations taken as part of the S2CLS survey (Geach et al. 2017) on the James Clark Maxwell Telescope. The S2CLS submillimeter map of the UDS field reaches a depth of $\sigma_{850} \sim 0.9\ \text{mJy}$ across $0.96\ \text{deg}^2$ with a typical beam of $\sim 15''$, and yields 716 submillimeter sources at $\geq 4\sigma$. In ALMA Cycle 1, Simpson et al. (2015) followed up 30 bright ($S_{870\ \mu\text{m}} \geq 8\ \text{mJy}$) submillimeter sources, taken from an early version of the S2CLS catalog at $\sim 0''.3$ resolution in Band 7 (870 μm). In 30 ALMA pointings, they found 52 SMGs with $S_{870\ \mu\text{m}} \geq 1\ \text{mJy}$ (with a median rms of $\sigma_{870\ \mu\text{m}} = 0.21\ \text{mJy beam}^{-1}$). Details of the pilot ALMA/SCUBA-2 UDS source catalog, data reduction, and imaging can be found in Simpson et al. (2015). The full sample of 716 SCUBA-2 sources—the AS2UDS sample—was subsequently observed with ALMA, and is presented in Stach et al. (2019).

2.2. Sample Selection and 1.4/6 GHz Radio Imaging

Of the 52 ALMA SMGs studied by Simpson et al. (2015), 29 are detected at $4\sigma \geq 25\ \mu\text{Jy}$ in deep 1.4 GHz VLA imaging of the UDS (V. Arumugam et al. 2019, in preparation). These 1.4 GHz observations were carried out under the VLA project A10108, and comprise a mosaic of 14 pointings, covering a $\sim 1.3\ \text{deg}^2$ region, centered on the UDS. With $\sim 160\ \text{hr}$ total on-source integration time in multiple array configurations (A, B, C, and D), the final 1.4 GHz image reaches a nearly constant rms noise $\sigma \sim 6\ \mu\text{Jy beam}^{-1}$ across the field (as low as $\sigma \sim 4\ \mu\text{Jy beam}^{-1}$ near the center of the mosaic), with a synthesized beam that is well characterized by a $1''.6$ Gaussian profile. A full description of the observations, data reduction, and

source catalog will be presented in V. Arumugam et al. (2019, in preparation).

Using the upgraded VLA between 2015 July and September (Project ID: 15A-249), we conducted a pilot study in A-configuration at the C-band toward the 10 SMGs with the brightest 1.4 GHz counterparts. We used the 3-bit receivers with a 2 s correlator read time, yielding instantaneous, full-polarization coverage from 4–8 GHz in 2 MHz wide channels. We hereafter refer to these observations by their central frequency, 6 GHz. Our observations comprise 70–150 minutes on source per field. We performed amplitude and bandpass calibration using a single 5 minute scan of 3C 48 at the beginning of each observing block, and derived phase solutions via a 70 s scan of the nearby phase reference source, J0215–0222, after each 270 s scan on the target.

We processed these new 6 GHz data using the Common Astronomy Software Applications (CASA; McMullin et al. 2007) version 5.1.0 and the included VLA Calibration Pipeline, however post-calibration inspection of the uv data revealed the presence of residual, strong radio frequency interference (RFI), most probably arising from geostationary satellites located in the Clarke Belt, whose declination range intersects the UDS field.²⁰ To mitigate this RFI, we passed the calibrated uv data for each target through the automated AOFLAGGER package developed for Low-Frequency Array (LOFAR; Offringa et al. 2012), and then performed a manual search for remaining low-level RFI using the CASA tool PLOTMS. To ease the computational burden of imaging the data without introducing significant smearing effects, we averaged the processed data in time (to an integration time of 3 s) but not in frequency. We imaged the data from each pointing to the half-power width of the primary beam ($\sim 8'$ per pointing) using WSCLEAN (Offringa et al. 2014) with natural weighting and a pixel scale of $0''.1$, which provides 3–5 pixels across the synthesized beam. Finally, we performed primary beam corrections and created image-plane mosaics from overlapping 6 GHz pointings using the *ATPS* task FLATN.

In addition to these new observations, the VLA has observed a further two deep adjacent pointings at 6 GHz within the Cosmic Assembly Near-infrared Deep Extragalactic Legacy Survey (CANDELS) region of the UDS field. The first of these pointings was observed under Project ID 12B-175 (PI: Rujopakam), and comprises approximately 50 hr on source, while the second pointing (15A-048: PI Tadaki) comprises $\sim 20\ \text{hr}$ on source. The pointing centers of these two images are separated by one half-power beamwidth. We retrieved the raw uv data for these projects from the VLA archive, and processed, calibrated, and imaged them following the same steps as outlined above.

The median rms of our targeted 6 GHz images is $\sigma_{6\text{ GHz}} = 4.8\ \mu\text{Jy beam}^{-1}$ ($2.7\ \mu\text{Jy beam}^{-1}$ near the pointing centers), while that of the deep mosaic made from archival data is $\sigma_{6\text{ GHz}} = 1.6\ \mu\text{Jy beam}^{-1}$ ($0.7\ \mu\text{Jy beam}^{-1}$ near the pointing centers).

While the 15A-249 VLA observations were devised as a follow-up to a subset of bright AS2UDS SMGs from the pilot study of Simpson et al. (2015), the subsequent analysis of the full AS2UDS catalog from Stach et al. (2019) revealed that 247 ALMA-detected SMGs lie within the combined footprint of our 12 6 GHz pointings. Of these 247 SMGs, 41 are detected at $\geq 5\sigma_{6\text{ GHz}}$ via blind source extraction using the AEGEAN source finder (Hancock et al. 2012), where σ is the local noise level

²⁰ <https://science.nrao.edu/facilities/vla/docs/manuals/obsguide/rfi>

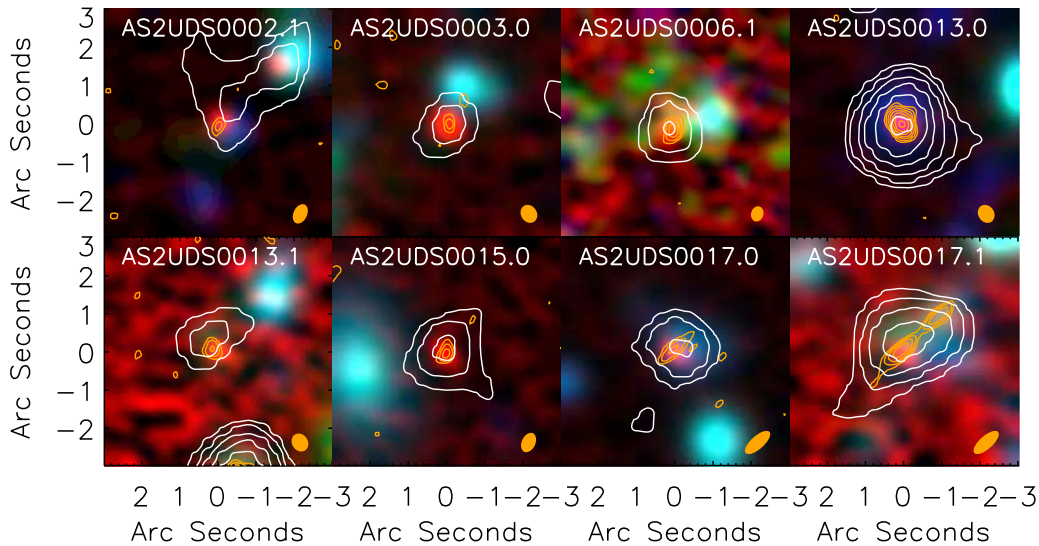


Figure 1. Postage stamp images of eight representative SMGs with $>5\sigma$ 6 GHz detections from our sample. False-color images are constructed from ALMA 870 μm (red), Subaru *i* (green), and V-band (blue) imaging, smoothed with a common $0''.35$ FWHM Gaussian kernel to highlight the complex morphology of the stellar continuum emission, and its offsets from the compact regions of dust-enshrouded star formation seen with ALMA. 6 GHz (orange) and 1.4 GHz (white) radio contours are plotted at $-3, 3, 3\sqrt{2} \times \sigma$ (and in steps of $\sqrt{2} \times \sigma$ thereafter). The 6 GHz sizes of our SMGs are on average $\sim (1.8 \pm 0.4) \times$ larger than the dust continuum sizes measured at 870 μm (which traces a region $\sim 2\text{--}3$ kpc in diameter), while at 1.4 GHz, a number of our sources appear to be marginally resolved on scales that can be probed by the VLA beam ($1''.6$, corresponding to physical sizes >10 kpc). Thumbnails for the remaining sources are shown in Appendix A.1, while the peculiar radio morphology of AS2UDS 0017.1 is discussed separately in Appendix A.4. We show the VLA 6 GHz synthesized beam as an orange ellipse in the bottom right corner of each panel.

obtained via boxcar smoothing the 6 GHz maps. We hereafter refer to these 41 SMGs as our 6 GHz SMG sample. We show false-color and radio continuum postage stamps of our 6 GHz-selected SMG sample in Figure 1.

2.3. GMRT 610 MHz

To study the low-frequency spectral properties of our SMG targets, we utilize a 610 MHz image of the UDS field obtained with GMRT. These data were obtained during 2006 February 3–6 and December 5–10, and the details of their reduction—along with a description of the imaging strategy—is presented in Ibar (2009) and Dunne et al. (2009).

Briefly, this GMRT map was formed from a three-pointing mosaic and comprises a total integration time of 12 hr per pointing, after setup/calibration overheads. The observing strategy employed 40 minute scans on the target field, interspersed with 5 minute scans of the bright phase calibrator, 0240–231. Flux and bandpass calibration were performed using the reference sources 3C 48 and 3C 147, respectively. Using 128×1.25 kHz channels in each of the two sidebands (centered at 602 and 618 MHz, respectively) and recording in dual polarization, the final mosaic reaches a typical sensitivity of $\sigma_{610 \text{ MHz}} \sim 60 \mu\text{Jy beam}^{-1}$ ($\sigma_{610 \text{ MHz}} \sim 40 \mu\text{Jy beam}^{-1}$ near the center of the field). The pixel scale of $1''.25$ well samples the GMRT 610 MHz synthesized beam ($\theta_{610 \text{ MHz}} \sim 5''$).

On visual inspection of our 870 μm /radio maps (Figure 1 and Appendix A.1), it is apparent that a significant number of our 6 GHz-selected SMGs have companion radio-emitting sources whose separation from the SMG is smaller than $5''$. As a result, the 610 MHz peak flux densities of these sources will be overestimated if we do not account for this source confusion. We deblended the GMRT image using the techniques previously outlined in Swinbank et al. (2014) and Thomson et al. (2017). Briefly, we extract a $15'' \times 15''$ thumbnail around each SMG from the GMRT image, and construct a model 610 MHz image of the same size, which we seed with delta functions at the positions of 870 μm -, 1.4

GHz-, and 6 GHz-detected sources (i.e., including all likely radio detections within each thumbnail regardless of whether or not they are associated with an SMG). Next, we assign random flux densities to each of the delta functions between 0 and $5 \times$ the peak in the GMRT postage stamp and convolve with the GMRT synthesized beam. We create a residual image by subtracting this model from the data, and measure the goodness of fit via the χ^2 statistic. We randomly perturb the flux densities assigned to the delta functions 100,000 times, or until χ^2 converges on a minimum. For SMGs that lie coincident with a $>3\sigma$ peak in the GMRT image and have no neighboring radio sources and/or SMGs within the GMRT beam, we measure the 610 MHz flux density directly from the peak pixel in the (non-deblended) GMRT thumbnail. For SMGs with $>3\sigma$ GMRT emission but nearby radio-detected or SMG companions that could be contributing to the observed flux density, we report flux densities from the corresponding deblended thumbnail. For SMGs that are not coincident with a GMRT source, we report 3σ upper limits based on the local noise level.

2.4. Size Measurements

We measure deconvolved angular sizes for our SMGs by fitting two-dimensional Gaussian models in the 1.4 and 6 GHz radio maps at the positions of the SMGs using the CASA task IMFIT. We report these sizes in Table 1. At the resolution of our GMRT map, we do not expect any of our SMGs to be resolved ($\theta_{610 \text{ MHz}} \sim 5''$ corresponds to a linear scale of ~ 40 kpc at $z \sim 2$), and so we do not perform forced Gaussian fitting to the 610 MHz map.

3. Results and Analysis

3.1. Radio Flux Densities and Spectral Indices

We create maps of the local rms and background from our three-band radio data using a custom IDL script, which boxcar smooths the maps, and performs blind source extraction on the 1.4 and 6 GHz images using the AEGEAN source finder (Hancock et al.

Table 1
Radio/Far-IR Properties of UDS SMGs—Flux Densities and Physical Sizes

ID ^a	$S_6 \text{ GHz}$ (μJy) ^b	$S_{1.4 \text{ GHz}}$ (μJy) ^b	$S_{610 \text{ MHz}}$ (μJy)	$S_{870 \mu\text{m}}$ (mJy)	z_{phot} ^c	$\theta_6 \text{ GHz}$ ($''$)	$\theta_{1.4 \text{ GHz}}$ ($''$)	$\theta_{870 \mu\text{m}}$ ($''$)
AS2UDS002.1 ^d	12 \pm 2	42 \pm 8	<220	7.4 \pm 0.5	3.35 \pm 0.24
AS2UDS003.0 ^d	13 \pm 2	50 \pm 8	<200	7.9 \pm 0.4	3.93 \pm 0.91	0.37 \pm 0.09
AS2UDS006.1 ^d	40 \pm 8 [6.8]	44 \pm 6	<140	2.3 \pm 0.4	3.28 \pm 0.30	0.53 \pm 0.14	...	0.88 \pm 0.28
AS2UDS013.0 ^e	58 \pm 4 [25.9]	251 \pm 22 [19.2]	350 \pm 69 ^f	6.2 \pm 0.3	2.04 \pm 0.09	0.30 \pm 0.06	1.06 \pm 0.28	...
AS2UDS013.1	12 \pm 2	55 \pm 10	<220	1.4 \pm 0.3	2.26 \pm 0.10
AS2UDS015.0	15 \pm 2	71 \pm 10	<390	5.6 \pm 0.5	6.53 \pm 0.54	0.53 \pm 0.13
AS2UDS017.0	16 \pm 2	77 \pm 10	<390	6.6 \pm 0.3	2.75 \pm 0.07	0.46 \pm 0.07
AS2UDS017.1	31 \pm 2	224 \pm 31	<390	1.5 \pm 0.4	1.26 \pm 0.15
AS2UDS021.0 ^e	136 \pm 5 [43.5]	753 \pm 30 [40.1]	1500 \pm 70	5.5 \pm 0.3	2.26 \pm 0.06	0.35 \pm 0.03	1.35 \pm 0.12	0.63 \pm 0.06
AS2UDS023.0 ^e	22 \pm 2	128 \pm 16 [12.6]	330 \pm 63	6.7 \pm 0.4	2.22 \pm 0.11	...	1.23 \pm 0.39	...
AS2UDS039.0	10 \pm 2	45 \pm 8	<280	5.8 \pm 0.3	2.94 \pm 0.10	0.47 \pm 0.08
AS2UDS056.1 ^{d,e}	153 \pm 13	401 \pm 16 [42.3]	410 \pm 77	2.0 \pm 0.6	3.17 \pm 0.07	...	0.81 \pm 0.15	...
AS2UDS064.0 ^{d,e}	126 \pm 4	641 \pm 20 [52.0]	1200 \pm 90	7.4 \pm 0.8	4.15 \pm 0.40	...	1.00 \pm 0.12	...
AS2UDS072.0 ^d	13 \pm 3	105 \pm 26 [5.6]	<220	8.2 \pm 0.8	2.88 \pm 0.12	...	2.72 \pm 0.83	...
AS2UDS082.0	13 \pm 3	36 \pm 7	<270	5.2 \pm 0.5	2.58 \pm 0.07	0.72 \pm 0.11
AS2UDS113.0 ^d	18 \pm 4 [6.4]	<22	<140	5.1 \pm 0.5	2.72 \pm 0.17	1.32 \pm 0.31	...	0.47 \pm 0.10
AS2UDS116.0	18 \pm 4 [6.2]	77 \pm 15 [7.8]	<150	6.0 \pm 0.6	2.44 \pm 0.29	0.75 \pm 0.18	1.97 \pm 0.59	0.49 \pm 0.13
AS2UDS125.0	30 \pm 2 [27.8]	114 \pm 13 [14.0]	<170	4.6 \pm 0.5	1.86 \pm 0.22	0.26 \pm 0.04	1.36 \pm 0.31	...
AS2UDS129.0	18 \pm 2	<50	630 \pm 140	5.2 \pm 0.7	2.75 \pm 0.29	0.52 \pm 0.16
AS2UDS137.0	26 \pm 2	104 \pm 8	300 \pm 69	5.9 \pm 0.4	2.62 \pm 0.01
AS2UDS238.0	35 \pm 7	31 \pm 8	<220	4.0 \pm 0.6	2.17 \pm 0.09	0.32 \pm 0.08
AS2UDS259.0	33 \pm 6 [8.4]	120 \pm 13 [14.5]	<140	4.7 \pm 0.3	1.86 \pm 0.04	0.47 \pm 0.13	1.27 \pm 0.29	0.33 \pm 0.09
AS2UDS265.0	10 \pm 2	43 \pm 7	<240	3.7 \pm 0.6	2.30 \pm 0.07
AS2UDS266.0	7 \pm 1	37 \pm 6	<130	4.2 \pm 0.7	2.75 \pm 0.25
AS2UDS272.0 ^e	90 \pm 2 [74.0]	260 \pm 12 [37.4]	220 \pm 54	5.1 \pm 0.5	1.78 \pm 0.21	0.40 \pm 0.01	0.70 \pm 0.20	...
AS2UDS283.0 ^e	24 \pm 5	116 \pm 22 [7.9]	280 \pm 67	3.9 \pm 0.7	1.88 \pm 0.12	...	2.02 \pm 0.58	0.85 \pm 0.21
AS2UDS297.0 ^e	27 \pm 3 [15.3]	104 \pm 15 [11.0]	200 \pm 49	4.4 \pm 0.6	1.68 \pm 0.20	0.46 \pm 0.07	1.91 \pm 0.42	...
AS2UDS305.0	13 \pm 2 [7.4]	30 \pm 7	<160	4.7 \pm 0.3	2.88 \pm 0.32	0.59 \pm 0.14	...	0.31 \pm 0.08
AS2UDS311.0	21 \pm 3 [8.4]	57 \pm 14 [6.2]	<140	5.8 \pm 0.8	2.14 \pm 0.10	0.59 \pm 0.13	1.94 \pm 0.64	0.54 \pm 0.17
AS2UDS407.0 ^g	15 \pm 2	54 \pm 7	<260	3.3 \pm 0.7	2.16 \pm 0.24
AS2UDS412.0	17 \pm 3 [6.0]	31 \pm 6	<140	4.1 \pm 0.3	2.60 \pm 0.19	0.74 \pm 0.19	...	0.47 \pm 0.09
AS2UDS428.0 ^e	98 \pm 6 [28.2]	404 \pm 18 [37.9]	560 \pm 69	4.7 \pm 0.8	1.67 \pm 0.04	0.26 \pm 0.06	0.90 \pm 0.14	0.55 \pm 0.16
AS2UDS460.1 ^e	19 \pm 2	131 \pm 18 [11.9]	370 \pm 84	3.1 \pm 0.7	2.74 \pm 0.16	...	1.28 \pm 0.36	...
AS2UDS483.0	17 \pm 2	128 \pm 23 [8.7]	<390	3.1 \pm 0.3	1.86 \pm 0.33	...	1.75 \pm 0.39	0.47 \pm 0.09
AS2UDS497.0	31 \pm 2	142 \pm 7	340 \pm 75	2.4 \pm 0.2	0.74 \pm 0.01	0.36 \pm 0.11
AS2UDS550.0 ^d	19 \pm 3	50 \pm 6	<210	4.9 \pm 0.5	3.05 \pm 0.17	0.62 \pm 0.12
AS2UDS590.0	9 \pm 2	<26	<210	3.3 \pm 0.3	2.42 \pm 0.11	0.42 \pm 0.11
AS2UDS608.0 ^{d,g}	50 \pm 9 [8.1]	144 \pm 9	<210	3.5 \pm 0.4	2.47 \pm 0.13	0.55 \pm 0.16
AS2UDS648.0	14 \pm 2	38 \pm 6	<190	1.8 \pm 0.5	2.48 \pm 0.05
AS2UDS665.0	11 \pm 2	32 \pm 7	<200	2.3 \pm 0.3	2.10 \pm 0.26
AS2UDS707.0 ^{d,g}	29 \pm 6 [6.2]	40 \pm 7	<290	2.2 \pm 0.3	2.53 \pm 0.15	0.58 \pm 0.14
Stack (all)	22 \pm 1	92 \pm 5	181 \pm 17	4.7 \pm 0.3	...	0.54 \pm 0.04	1.36 \pm 0.16	0.28 \pm 0.06
Stack (bright)	21 \pm 5	152 \pm 6	291 \pm 18	5.1 \pm 0.4	...	0.63 \pm 0.04	1.10 \pm 0.13	0.22 \pm 0.05
Stack (faint)	20 \pm 5	49 \pm 5	93 \pm 12	4.2 \pm 0.4	...	0.49 \pm 0.08	1.26 \pm 0.29	0.33 \pm 0.07
Stack (convex)	56 \pm 2	262 \pm 7	430 \pm 24	5.1 \pm 0.1	...	0.51 \pm 0.03	1.03 \pm 0.14	0.20 \pm 0.04

Notes.

^a IDs follow those of Stach et al. (2019), and differ from those of Simpson et al. (2015), which were based on a preliminary version of the AS2UDS sample.

^b For unresolved sources we report peak flux densities and uncertainties. For spatially resolved sources we report the fitted (integrated) flux densities and uncertainties, and report the peak S/N in square brackets for reference.

^c Photometric redshifts are obtained via multiband SED fits to the UKIDSS UDS DR11 catalog (O. Almaini et al. 2019, in preparation; U. Dudzevičiūtė et al. 2019, in preparation).

^d Candidate AGN host based on *Spitzer* IRAC colors.

^e Candidate AGN host based on X-ray detection.

^f GMRT flux density measured from deblended thumbnail.

^g Source is detected in all three radio bands and has a convex spectrum, i.e., $\alpha_{610 \text{ MHz}}^{1.4 \text{ GHz}} > \alpha_{1.4 \text{ GHz}}^{6 \text{ GHz}}$.

2012). We employ a local 5σ threshold to define peaks in the image, and then perform two-dimensional Gaussian fits to these peaks using the CASA task IMFIT, yielding both total/peak flux densities and fitted/deconvolved source sizes. Next, we isolate the radio counterparts to SMGs by crossmatching the resulting 1.4 and

6 GHz catalogs to the AS2UDS 870 μm catalog with a $1''$ search radius. For SMGs that lack a radio counterpart in one or more bands, we measure a 3σ upper limit to the radio flux density (assuming the source is unresolved) from the corresponding local rms map. As discussed in Section 2.3, we measure GMRT flux

Table 2
The Far-IR/Radio Correlation and Cosmic-Ray Electron Diffusion

ID	$\alpha_{1.4\text{ GHz}}^6\text{ GHz}^a$	$\alpha_{610\text{ MHz}}^{1.4\text{ GHz}}^a$	q_{IR}^b	n_{H} (cm^{-3})	B (μG)	$\tau_{\text{cool,min}}$ ($\times 10^4\text{ yr}$)	$\tau_{\text{cool,max}}$ ($\times 10^4\text{ yr}$)	$l_{\text{cool,min}}$ (pc)	$l_{\text{cool,max}}$ (pc)
AS2UDS002.1 ^c	-0.87 ± 0.17	> -1.99	2.7 ± 0.5	15 ± 3	40 ± 5	3 ± 1	12 ± 5	120 ± 30	230 ± 50
AS2UDS003.0 ^c	-0.89 ± 0.16	> -1.68	2.1 ± 0.5	23 ± 7	50 ± 5	3 ± 2	19 ± 13	120 ± 40	290 ± 100
AS2UDS006.1 ^c	-0.07 ± 0.16	> -1.41	2.1 ± 0.4	4 ± 1	20 ± 5	23 ± 11	33 ± 15	350 ± 80	410 ± 100
AS2UDS013.0 ^d	-1.01 ± 0.08	-0.40 ± 0.22	2.5 ± 0.2	13 ± 1	35 ± 5	5 ± 1	18 ± 2	150 ± 10	270 ± 20
AS2UDS013.1	-1.07 ± 0.17	> -1.67	1.9 ± 0.3	3 ± 1	20 ± 5	30 ± 8	90 ± 26	380 ± 60	670 ± 100
AS2UDS015.0	-1.06 ± 0.13	> -2.05	1.5 ± 0.4	11 ± 4	35 ± 5	3 ± 2	17 ± 14	120 ± 50	300 ± 130
AS2UDS017.0	-1.09 ± 0.13	> -1.95	2.1 ± 0.2	9 ± 1	30 ± 5	8 ± 1	30 ± 5	190 ± 20	370 ± 30
AS2UDS017.1	-1.36 ± 0.10	> -0.67	2.2 ± 0.4	4 ± 1	20 ± 5	20 ± 10	68 ± 34	300 ± 80	550 ± 140
AS2UDS021.0 ^d	-1.18 ± 0.04	-0.83 ± 0.06	1.7 ± 0.1	12 ± 4	35 ± 5	8 ± 3	17 ± 7	180 ± 40	270 ± 60
AS2UDS023.0 ^d	-1.22 ± 0.10	-1.13 ± 0.23	1.9 ± 0.2	19 ± 2	45 ± 5	13 ± 4	33 ± 9	230 ± 30	360 ± 50
AS2UDS039.0	-1.02 ± 0.17	> -2.21	2.5 ± 0.2	12 ± 2	35 ± 5	6 ± 1	22 ± 5	160 ± 20	310 ± 30
AS2UDS056.1 ^{c,d}	-0.66 ± 0.06	-0.04 ± 0.19	1.9 ± 0.1	4 ± 1	20 ± 5	6 ± 0	21 ± 1	170 ± 0	330 ± 10
AS2UDS064.0 ^{c,d}	-1.12 ± 0.03	-0.76 ± 0.08	0.9 ± 0.1	27 ± 6	50 ± 5	8 ± 4	20 ± 9	180 ± 40	290 ± 70
AS2UDS072.0 ^c	-1.42 ± 0.21	> -0.87	2.1 ± 0.2	20 ± 2	45 ± 5	8 ± 2	24 ± 5	190 ± 20	320 ± 30
AS2UDS082.0	-0.71 ± 0.19	> -2.42	2.5 ± 0.3	14 ± 2	35 ± 5	21 ± 6	33 ± 9	300 ± 40	370 ± 50
AS2UDS113.0 ^c	> -0.13	21 ± 3	45 ± 5	11 ± 4	30 ± 11	210 ± 40	350 ± 70
AS2UDS116.0	-0.99 ± 0.19	> -0.83	2.3 ± 0.2	16 ± 1	40 ± 5	11 ± 1	30 ± 2	210 ± 10	350 ± 10
AS2UDS125.0	-0.92 ± 0.09	> -0.46	2.4 ± 0.4	18 ± 4	45 ± 5	15 ± 7	36 ± 18	240 ± 60	380 ± 100
AS2UDS129.0	> -0.71	11 ± 3	35 ± 5	10 ± 5	29 ± 14	210 ± 50	360 ± 90
AS2UDS137.0	-0.97 ± 0.07	-1.27 ± 0.24	2.0 ± 0.3	9 ± 1	30 ± 5	6 ± 2	22 ± 8	170 ± 30	310 ± 60
AS2UDS238.0	0.08 ± 0.22	> -2.34	2.4 ± 0.3	14 ± 3	40 ± 5	10 ± 4	47 ± 17	210 ± 40	440 ± 80
AS2UDS259.0	-0.89 ± 0.14	> -0.20	2.5 ± 0.1	15 ± 3	40 ± 5	8 ± 2	38 ± 9	180 ± 20	390 ± 50
AS2UDS265.0	-0.98 ± 0.17	> -2.03	2.2 ± 0.2	14 ± 2	35 ± 5	20 ± 4	47 ± 10	290 ± 30	450 ± 50
AS2UDS266.0	-1.18 ± 0.14	> -1.54	2.1 ± 0.3	15 ± 4	40 ± 5	19 ± 8	43 ± 20	280 ± 70	430 ± 100
AS2UDS272.0 ^d	-0.73 ± 0.04	0.21 ± 0.25	2.4 ± 0.4	20 ± 5	45 ± 5	14 ± 7	35 ± 17	230 ± 60	370 ± 90
AS2UDS283.0 ^d	-1.10 ± 0.19	-1.04 ± 0.31	2.0 ± 0.2	12 ± 2	35 ± 5	39 ± 12	44 ± 13	400 ± 60	430 ± 70
AS2UDS297.0 ^d	-0.93 ± 0.12	-0.80 ± 0.28	2.2 ± 0.1	12 ± 1	35 ± 5	19 ± 2	50 ± 6	280 ± 20	450 ± 30
AS2UDS305.0	-0.58 ± 0.20	> -1.98	2.4 ± 0.5	12 ± 2	35 ± 5	4 ± 2	33 ± 15	140 ± 30	380 ± 90
AS2UDS311.0	-0.69 ± 0.21	> -1.11	2.3 ± 0.3	18 ± 2	40 ± 5	21 ± 5	39 ± 9	290 ± 30	400 ± 40
AS2UDS407.0 ^c	-0.89 ± 0.13	> -1.88	2.1 ± 0.3	10 ± 2	30 ± 5	24 ± 9	59 ± 23	320 ± 60	500 ± 100
AS2UDS412.0	-0.40 ± 0.19	> -1.78	2.4 ± 0.3	11 ± 2	35 ± 5	14 ± 4	41 ± 13	250 ± 40	430 ± 70
AS2UDS428.0 ^d	-0.98 ± 0.05	-0.39 ± 0.13	2.0 ± 0.1	15 ± 1	40 ± 5	20 ± 1	40 ± 2	280 ± 10	390 ± 10
AS2UDS460.1 ^d	-1.32 ± 0.11	-1.26 ± 0.26	1.0 ± 0.1	6 ± 3	25 ± 5	35 ± 28	88 ± 69	410 ± 170	650 ± 270
AS2UDS483.0	-1.40 ± 0.16	> -1.33	1.8 ± 0.3	12 ± 2	35 ± 5	28 ± 12	60 ± 26	340 ± 70	490 ± 110
AS2UDS497.0	-1.04 ± 0.06	-1.06 ± 0.22	2.5 ± 0.1	7 ± 1	25 ± 5	24 ± 2	103 ± 7	300 ± 10	630 ± 20
AS2UDS550.0 ^c	-0.65 ± 0.13	> -1.75	2.4 ± 0.2	9 ± 2	30 ± 5	8 ± 2	20 ± 5	200 ± 20	310 ± 40
AS2UDS590.0	> -0.75	15 ± 2	40 ± 5	31 ± 9	61 ± 18	360 ± 50	510 ± 70
AS2UDS608.0 ^{c,e}	-0.73 ± 0.14	> -0.45	2.1 ± 0.1	14 ± 8	40 ± 10	12 ± 11	33 ± 29	220 ± 100	370 ± 170
AS2UDS648.0	-0.66 ± 0.14	> -1.94	2.2 ± 0.2	4 ± 2	20 ± 5	19 ± 13	60 ± 40	310 ± 110	540 ± 190
AS2UDS665.0	-0.73 ± 0.17	> -2.21	2.4 ± 0.4	6 ± 1	25 ± 5	24 ± 9	69 ± 25	330 ± 60	560 ± 100
AS2UDS707.0 ^{c,e}	-0.22 ± 0.18	> -2.38	2.7 ± 0.3	12 ± 2	35 ± 5	13 ± 4	36 ± 10	230 ± 30	390 ± 60
Stack (all)	-0.98 ± 0.07	-0.81 ± 0.11	2.20 ± 0.13	10 ± 1	35 ± 1	4.2 ± 0.6	35.9 ± 5.5	130 ± 10	390 ± 30
Stack (bright)	-1.35 ± 0.24	-0.79 ± 0.07	2.14 ± 0.15	10 ± 1	35 ± 2	2.8 ± 0.6	35.8 ± 7.3	110 ± 10	390 ± 40
Stack (faint)	-0.81 ± 0.11	-0.77 ± 0.16	2.49 ± 0.23	10 ± 1	35 ± 2	5.8 ± 1.4	35.6 ± 8.4	160 ± 20	390 ± 50
Stack (convex)	-1.06 ± 0.04	-0.60 ± 0.06	2.20 ± 0.27	10 ± 2	35 ± 3	2.7 ± 0.9	35.3 ± 11.5	110 ± 20	380 ± 60

Notes.

^a Spectral index limits between two frequencies with one detection are determined by setting the flux density of the non-detection to 3σ . It is not possible to constrain the spectral index between two non-detections.

^b Where $\alpha_{610\text{ MHz}}^{1.4\text{ GHz}}$ is constrained by a 1.4 GHz detection and a 610 MHz upper limit, we measure q_{IR} by assuming a canonical $\alpha_{610\text{ MHz}}^{1.4\text{ GHz}} = -0.8$, providing this assumption is consistent with the 3σ flux density limits.

^c Have the same meaning as in Table 1.

^d Have the same meaning as in Table 1.

^e Have the same meaning as in Table 1.

densities from the peak pixel value at the position of the SMG using either the raw or deblended image, depending on the number of probable confusing sources nearby.

The three-band radio flux densities (and upper limits) of our 6 GHz-selected SMGs are reported in Table 1, with the measured spectral indices (or spectral index limits, in the case of sources that are undetected in one of the two radio bands) shown in Table 2.

We measure the spectral indices in two frequency ranges, from 610 MHz–1.4 GHz ($\alpha_{610\text{ MHz}}^{1.4\text{ GHz}}$) and from 1.4–6 GHz ($\alpha_{1.4\text{ GHz}}^6\text{ GHz}$). The median 1.4 GHz flux density of our sample is $\langle S_{1.4\text{ GHz}} \rangle = 92 \pm 5 \mu\text{Jy}$.

Twelve of our SMGs are detected in all three radio bands, with a median spectral index $\langle \alpha_{610\text{ MHz}}^{1.4\text{ GHz}} \rangle = -0.80 \pm 0.14$, which is consistent with the typical spectral indices seen at

these frequencies in previous SMG studies (e.g., Ibar et al. 2010; Thomson et al. 2014), and with measurements of the (synchrotron-dominated) low-frequency radio spectral indices in local starbursts (e.g., M82: Condon 1992) and low-SFR high-redshift sources (Murphy et al. 2017).

Turning to higher frequencies, the 41 SMGs detected at 6 GHz have a median flux density $S_{6\text{ GHz}} = 22 \pm 1 \mu\text{Jy}$. Prior to analyzing the maps, we anticipated that the 6 GHz flux densities would be $\sim 50\%$ higher than this, owing to the combination of synchrotron emission (extrapolated from their previously measured 1.4 GHz flux densities assuming a typical spectral index $\alpha_{\text{sync}} = -0.8$) plus thermal free-free emission, which we expected to contribute an additional $\sim 10\text{--}20 \mu\text{Jy}$, given the high SFRs estimated from the far-IR SED fits ($\text{SFR}_{\text{IR}} \sim 500 M_{\odot} \text{ yr}^{-1}$), leading to a predicted $\alpha_{1.4\text{ GHz}}^{6\text{ GHz}} \gtrsim -0.5$. In fact, the flux densities of our 6 GHz sample result in a median high-frequency spectral index $\langle \alpha_{1.4\text{ GHz}}^{6\text{ GHz}} \rangle = -0.93 \pm 0.05$, which is slightly steeper than the low-frequency spectral index for the whole sample, and suggests there is no evidence of the expected flattening of the spectrum at higher frequency due to thermal free-free emission. Similar spectral behavior has also recently been reported in 310 MHz–3 GHz observations undertaken by the VLA follow-up of the Cosmological Evolution Survey (COSMOS) field 3 GHz Large Project (Tisanić et al. 2019), which attributes the effect to lower-than-expected thermal free-free emission (see also Barcos-Muñoz et al. 2015).

Given this somewhat unexpected finding, we performed a series of consistency checks to test the accuracy of our flux density measurements, using both the processed VLA uv data and also simulated uv data sets representing “observations” of model galaxies of known size/flux density under the same conditions as those of the real observations. Details of these tests are given in Appendix A.2. In summary, we find no evidence that the lower-than-expected 6 GHz flux densities are the result of either instrumental effects, or systematic problems, with the calibration of the flux density scale.

3.2. Stacking Analysis

To check that the observed spectral behavior is not a spurious result driven by low signal-to-noise (S/N) detections, we perform a stacking analysis. We stack our 1.4 GHz and 610 MHz data in the image plane by extracting $20''$ thumbnails around each SMG. We resample these thumbnails 100 times, measuring the median flux density in each pixel, and then create final, stacked thumbnails by computing the “median of the medians” of these 100 stacked subsamples. At 610 MHz, we extract thumbnails from the published map (Ibar 2009) for SMGs with no 1.4 GHz or SMG companions within $5''$ (corresponding to the GMRT synthesized beam). For SMGs with nearby companions that may be contributing to the 610 MHz flux density at the position of the SMG, we use thumbnails extracted from the deblended model image (Section 2.3) with the nearby sources removed.

In addition to creating median stacks, we also create error images for each of the stacks by computing in each pixel the standard deviation of the bootstrap-resampled thumbnails used in the stacking procedure. We measure uncertainties in our stacked flux densities from these maps by measuring the peak pixel value within $1''$ of the centroid of the error image.

At 6 GHz and $870 \mu\text{m}$, our sources are not cropped from a single wide-field image with a stable point-spread function (PSF)

but were observed in multiple pointings, over a range of elevations and with different beam shapes. As a result, simple image-plane stacking of the kind performed in the 610 MHz and 1.4 GHz maps would be inappropriate, as the flux density units of our maps are Jy beam^{-1} , and the beam varies from pointing to pointing. We therefore employ the STACKER library developed for use in CASA (Lindroos et al. 2015) to generate median 6 GHz and $870 \mu\text{m}$ stacks in the uv plane, from which we then create stacked images using CASA TCLEAN; by stacking the data in the uv plane and then performing a single imaging run (with a single, well-defined PSF) on the gridded, stacked uv data we are able to circumvent issues that would otherwise arise from the inhomogeneous PSFs of our individual 6 GHz and $870 \mu\text{m}$ maps.

In order to search for evolution in the spectral properties of our SMGs as a function of radio flux density, we generate stacks for the entire sample of 41 6 GHz-detected SMGs, as well as for samples comprised of SMGs above and below the median 1.4 GHz flux density, which we label the “all,” “bright,” and “faint” stacks, respectively. In addition, to further investigate the unexpected spectral index curvature seen in the 10/12 SMGs with detections in three radio bands, we create an additional stack comprised of those SMGs with $\alpha_{610\text{ MHz}}^{1.4\text{ GHz}} > \alpha_{1.4\text{ GHz}}^{6\text{ GHz}}$. We label this the “convex” subsample. We show individual SEDs for the 12 SMGs detected in all three radio bands in Figure 2, along with the convex-stacked SED, and show stacked thumbnail images from the convex sample in Figure 3.

The bright and faint stacked subsamples have high-frequency spectral indices of $\alpha_{1.4\text{ GHz}}^{6\text{ GHz}} = -1.35 \pm 0.24$ and $\alpha_{1.4\text{ GHz}}^{6\text{ GHz}} = -0.81 \pm 0.11$ and low-frequency spectral indices of $\alpha_{610\text{ MHz}}^{1.4\text{ GHz}} = -0.79 \pm 0.07$ and $\alpha_{610\text{ MHz}}^{1.4\text{ GHz}} = -0.77 \pm 0.16$, respectively, suggesting that brighter SMGs may have intrinsically steeper spectra between rest frame $\sim 3\text{--}20$ GHz than they do at lower frequencies. For the convex subset (representing around $\sim 25\%$ of our 6 GHz SMG sample) we measure $\alpha_{1.4\text{ GHz}}^{6\text{ GHz}} = -1.06 \pm 0.04$ and $\alpha_{610\text{ MHz}}^{1.4\text{ GHz}} = -0.60 \pm 0.06$, a $\gtrsim 4\sigma$ difference in the low- and high-frequency spectral indices in this subsample.²¹ If the radio emission at all three frequencies shares a common origin (i.e., synchrotron and free-free emission from current star formation), then the implication of this spectral steepening is that either the synchrotron or free-free components (or conceivably both) are suppressed at higher frequency, relative to simple extrapolations from lower frequency emission. Alternatively, the high- and low-frequency radio emission in these SMGs may arise from decoupled processes, in which case the curvature seen in the source-integrated radio SEDs may arise from the mixing of emission from processes that dominate in different frequency ranges and potentially on different physical scales. We will return to this idea in Section 4.3.

The measured low- and high-frequency spectral indices of our sample (including stacked subsamples) are shown in Figure 4.

3.3. The Far-infrared/Radio Correlation

To measure the rest-frame radio luminosities ($L_{1.4\text{ GHz}}$) of our sample, we must first k -correct the observed frame 1.4 GHz

²¹ We note that by definition all 41 6 GHz-selected SMGs are detected at 6 GHz, of which the majority (38/41) are also detected at 1.4 GHz. The 610 MHz detection rate is 13/41, which suggests that any potential issues due to flux boosting from low S/N detections are more likely to affect $S_{610\text{ MHz}}$ than $S_{6\text{ GHz}}$. If $S_{610\text{ MHz}}$ is systematically overestimated due to flux-boosting effects, then this would artificially *reduce* the strength of the spectral break rather than cause it.

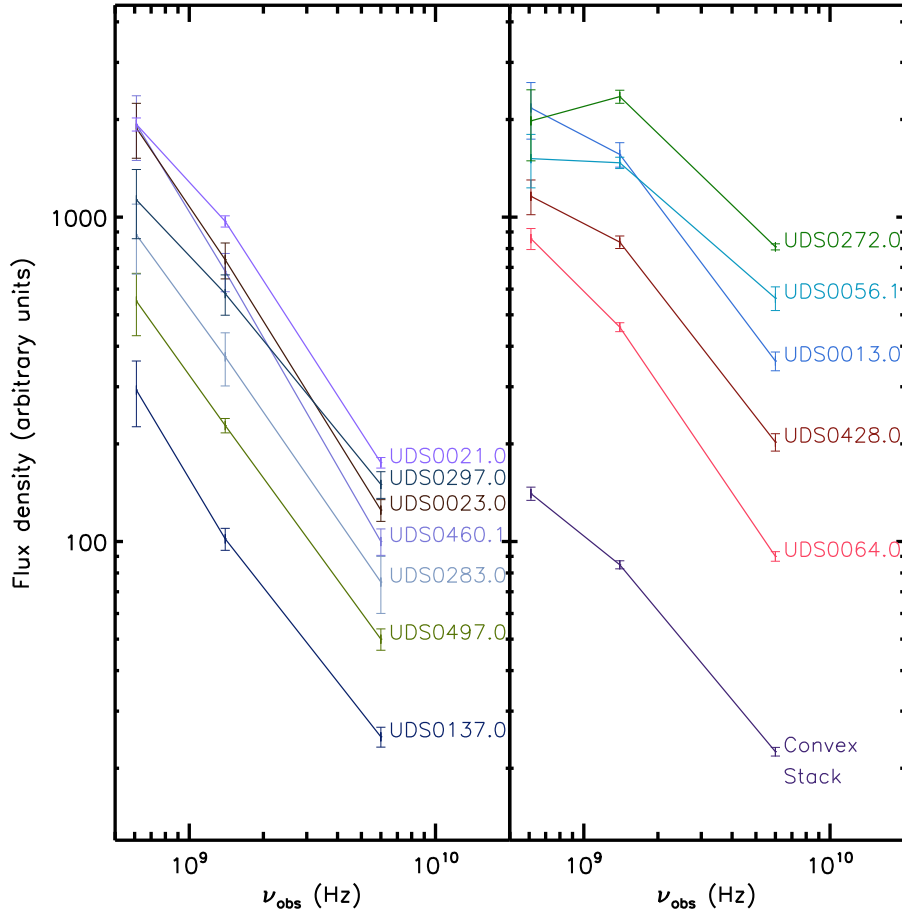


Figure 2. Observed-frame radio SEDs for the 12 SMG targets detected at 610 MHz, 1.4 GHz, and 6 GHz, ranked by the strength of the observed spectral break, $|\alpha_{1.4\text{ GHz}}^{6\text{ GHz}} - \alpha_{610\text{ MHz}}^{1.4\text{ GHz}}|$, with the seven SMGs showing the weakest break shown in the left panel and the six SMGs showing the strongest break shown in the right panel. The SEDs have been arbitrarily re-normalized in flux to allow them to be plotted on the same panels, facilitating a comparison of their spectral shapes. Prior to conducting the 6 GHz observations, our expectation was that the radio SEDs would flatten at higher frequency due to the increasing contribution of thermal free-free emission at $\nu_{\text{rest}} \gtrsim 10$ GHz (e.g., Condon 1992; Murphy et al. 2017), however we failed to observe significant spectral flattening in 10/12 SMGs with sufficient radio luminosities to be detected in all three radio bands. To illustrate that this apparent spectral steepening (or lack of expected spectral flattening) is not simply driven by low S/N maps, we also include a stacked SED of these 10 SMGs in the right panel (the convex SMG sample, which has $\alpha_{1.4\text{ GHz}}^{6\text{ GHz}} = -1.06 \pm 0.04$ and $\alpha_{610\text{ MHz}}^{1.4\text{ GHz}} = -0.60 \pm 0.06$).

flux densities:

$$L_{1.4\text{ GHz, rest}} \equiv L_{1.4\text{ GHz}} = 4\pi D_L^2 S_{1.4\text{ GHz, obs}} (1+z)^{-1-\alpha}, \quad (1)$$

where D_L is the luminosity distance to the source, and the subscripts “rest” and “obs” denote rest-frame and observed-frame quantities, respectively.

Our three-band radio photometry provides independent spectral indices on either side of $\nu_{\text{obs}} = 1.4$ GHz. Emission from *rest frame* 1.4 GHz in a $z \sim 2.3$ galaxy is shifted to lower frequencies (~ 400 MHz), while emission at *observed* 1.4 GHz was originally emitted at higher frequency in the rest frame. Therefore to obtain rest frame 1.4 GHz flux densities from observed frame $S_{1.4\text{ GHz}}$ in the presence of spectral curvature, the appropriate spectral index to use is $\alpha_{610\text{ MHz}}^{1.4\text{ GHz}}$. Because the majority of our 6 GHz SMG sample lack a $>3\sigma$ detection in the GMRT 610 MHz image, we can only set lower limits on $\alpha_{610\text{ MHz}}^{1.4\text{ GHz}}$ for these sources. Where these lower limits are consistent with the sample median ($\alpha_{610\text{ MHz}}^{1.4\text{ GHz}} = -0.84 \pm 0.10$), we k -correct using this spectral index, and where the 3σ GMRT flux limits necessitate a flatter spectral index than the sample median, we k -correct using the corresponding 3σ spectral index limit (Table 2).

In U. Dudzevičiūtė et al. (2019, in preparation), we measure the photometric redshifts of our SMGs via SED fits to the multiband

photometry in the UDS field (*UBVRIZYJHK*, Infrared Array Camera (IRAC) 3.6, 4.5, 5.8, 8.0 μm , MIPS 24 μm , *Herschel* PACS 100, 160 μm , deblended SPIRE 250, 350, 500 μm , ALMA 870 μm , and VLA 1.4 GHz) obtained using the MAGPHYS code (da Cunha et al. 2008). MAGPHYS employs the stellar population synthesis models of Bruzual & Charlot (2003) with a Chabrier (2003) stellar initial mass function (IMF) combined with a two-component dust attenuation model (Charlot & Fall 2000), balancing the energetics between the mid- and far-IR dust components to disentangle the integrated dust-attenuated stellar emission of the galaxy and the dust-reprocessed stellar emission. From these SED fits we also obtain rest frame 8–1000 μm luminosities, L_{IR} . Full details of the MAGPHYS SED fitting and the resulting multiwavelength properties will be described in U. Dudzevičiūtė et al. (2019, in preparation). We now use these measurements of L_{IR} in conjunction with the rest-frame radio luminosities to study the far-IR/radio correlation, via the parameter:

$$q_{\text{IR}} = \log \left[\frac{L_{\text{IR}}}{3.75 \times 10^{12} \text{ W}} \times \frac{\text{W Hz}^{-1}}{L_{1.4\text{ GHz}}} \right], \quad (2)$$

as in Ivison et al. (2010).

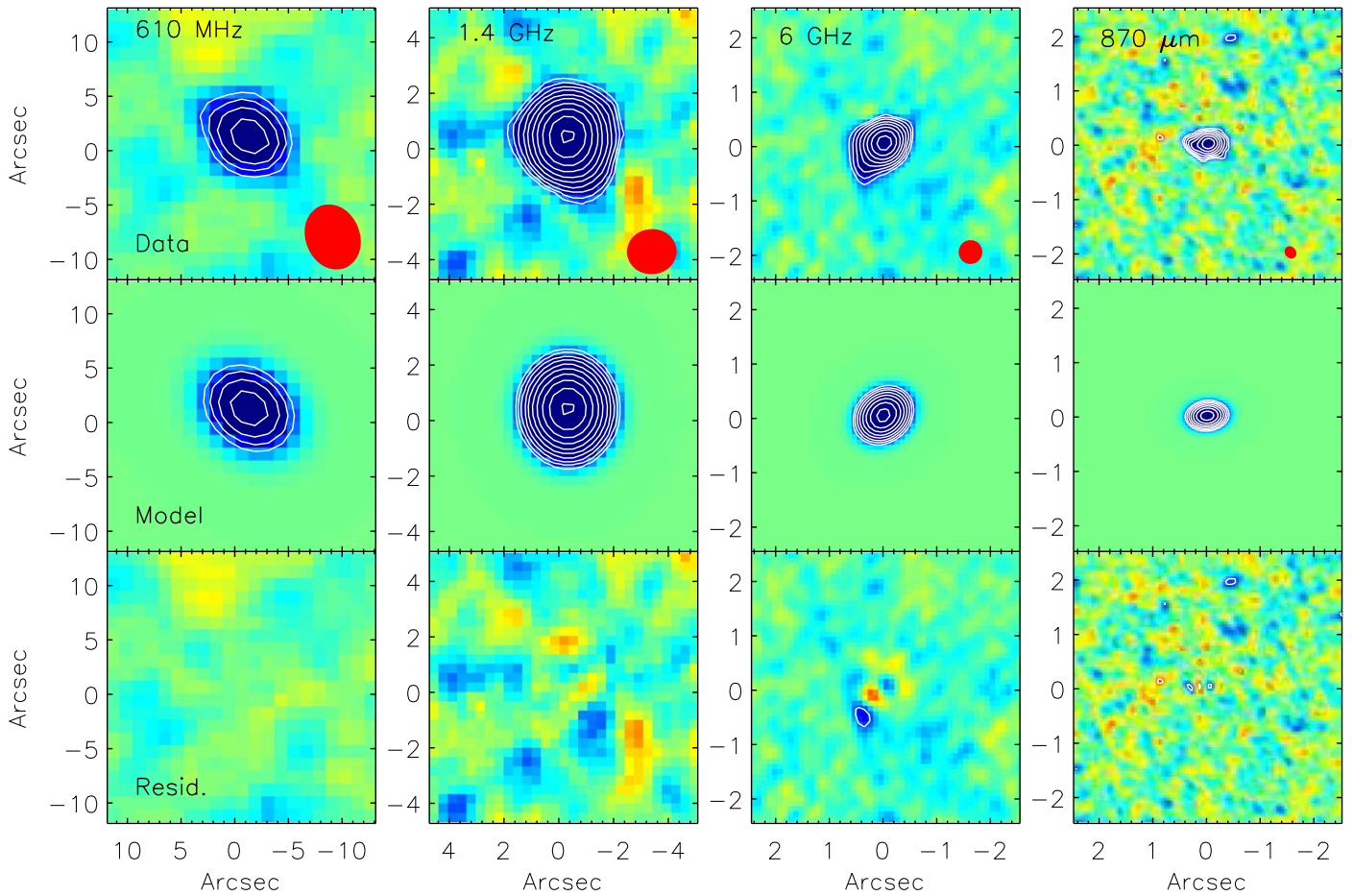


Figure 3. Top: false-color stacked thumbnail images at 610 MHz, 1.4 GHz, 6 GHz, and 870 μm for the sample of 10 SMGs exhibiting a clear break in their radio spectra at approximately gigahertz frequencies (i.e., the convex sample), with white contours over-plotted at $-3, 3, \sqrt{2} \times \sigma$ (and in steps of $\sqrt{2} \times \sigma$ thereafter), where σ is the local rms within each thumbnail image ($\sigma_{610 \text{ MHz}} = 37 \mu\text{Jy beam}^{-1}$; $\sigma_{1.4 \text{ GHz}} = 3.5 \mu\text{Jy beam}^{-1}$; $\sigma_{6 \text{ GHz}} = 0.8 \mu\text{Jy beam}^{-1}$; $\sigma_{870 \mu\text{m}} = 57 \mu\text{Jy beam}^{-1}$). Note the difference in the angular sizes of these thumbnails; we show the PSF corresponding to each image as a red-filled circle in the bottom right of the panels in the top row. The color scale of the thumbnail images runs between $\pm 5\sigma$. Middle: single-component two-dimensional Gaussian model fits to the thumbnail images obtained using the CASA task IMFIT, shown with the same color stretch and contour spacing as for the data. Note that the model images are not deconvolved from the PSF, however the angular sizes reported in Table 1 are. Unsurprisingly, at the angular resolution of our 610 MHz map ($\sim 5''$) the best-fit model is an unresolved point source. At 1.4 GHz, however, the angular resolution ($\sim 1''.6$) and high S/N of our stacked thumbnail (S/N ~ 35) allows a resolved source model to be fit with a deconvolved major axis $\theta_{6 \text{ GHz}} \sim 1''.06 \pm 0.22$. Likewise at 6 GHz and 870 μm we measure deconvolved source sizes of $\theta_{6 \text{ GHz}} = 0''.68 \pm 0''.05$ and $\theta_{870 \mu\text{m}} = 0''.24 \pm 0''.05$, from images with peak S/N ~ 21 and ~ 25 , respectively. Bottom: residual images (i.e., data-model) for the four stacked thumbnail images, again shown with the same color stretch and contour spacing as for the original thumbnails. The 610 MHz and 1.4 GHz residual thumbnail images are noise-like, as are the 6 GHz and 870 μm residual thumbnail images (save for a single beam-sized 3σ peak in the former image and four sub-beam-sized 3σ peaks in the latter image), highlighting that the single-component Gaussian fits (and the sizes measured from them) well characterize the two-dimensional flux distributions of our convex-stacked sample.

We measure a median $\langle q_{\text{IR}} \rangle = 2.20 \pm 0.06$ for the 6 GHz- and 1.4 GHz-detected SMGs (Table 2), a little lower than that measured in a sample of 52 radio-detected ALMA SMGs from the ECDFS field ($q_{\text{IR}} = 2.56 \pm 0.05$; Thomson et al. 2014), a result that is likely driven by our 6 GHz selection criterion.

Four of our SMGs have $q_{\text{IR}} < 1.7$, which marks the classical cutoff between star formation-dominated and “radio-excess” (i.e., AGN-dominated) sources (e.g., Del Moro et al. 2013)—however, none of these SMGs has a bright X-ray counterpart, either in the 1.3 deg^2 *XMM* SXDS catalog (Ueda et al. 2008), or in the deeper *Chandra* coverage (Kocevski et al. 2018), and thus if these radio-excess sources host active nuclei, they are likely to be Compton thick. Ten of our SMGs have mid-IR colors consistent with a dusty torus (e.g., Donley et al. 2012), of which two also fit the radio-excess ($q_{\text{IR}} \lesssim 1.7$) criterion. 15/41 SMGs ($\sim 37\%$ of our sample) satisfy at least one of the radio excess, X-ray detection, or IRAC color-color criteria, highlighting them as possible AGN, however we note that dust-reddened stellar SEDs of high-redshift starburst

galaxies can be mistaken for AGN in simple color classification schemes (e.g., Radcliffe et al. 2019). No sources meet all three AGN criteria, however three (AS2UDS064.0, 608.0, and 707.0) meet two AGN criteria. In addition to q_{IR} values, we also highlight in Table 2 which sources meet the IRAC color-color criterion for AGN and which are X-ray detected.

3.4. The Sizes and Morphologies of SMGs

We now compare our measured radio sizes with the 870 μm dust sizes of our sample from Stach et al. (2019).

We find that 15/41 SMGs are formally resolved at $>3\sigma$ significance (i.e., $\theta/\delta\theta \geq 3$) in our CASA IMFIT measurements at 6 GHz. However, deconvolved size measurements for compact sources (i.e., close to the beam size) must be interpreted with caution, as they may be susceptible to spurious source broadening due to correlated noise in the image and/or residual calibration errors. As a result, at low S/N even point sources may be spuriously fit as extended sources. To account

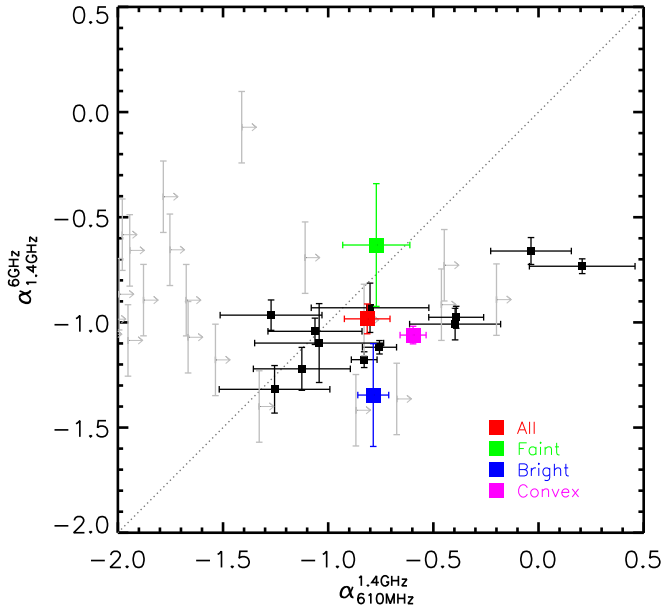


Figure 4. A comparison between the high- and low-frequency radio spectral indices of our 6 GHz-selected SMG sample, including the 13 SMGs with detections in all three radio bands, 26 with detections at 1.4 and 6 GHz (i.e., with measured high-frequency spectral indices but only 3σ limits on their low-frequency spectral indices) and each of the stacked subsamples outlined in Section 3.2. In local starburst galaxies and $\sim\mu\text{Jy}$ radio galaxies at high-redshift, steep-spectrum synchrotron emission dominates at low frequency and gives way at higher frequency to the flatter spectrum free-free emission (e.g., Condon 1992; Murphy et al. 2017). In this scenario, we would expect star-forming galaxies to lie above the 1:1 line. Instead, for those SMGs that are bright enough to have their spectral indices measured across two frequency intervals, we see a tendency for their SEDs to *steepen* at higher frequency.

for this effect, we ran a suite of simulations using the CASA task SIMOBSERVE for 10,000 point-source models with uv coverage similar to that of our real 6 GHz observations, created maps and catalogs from these simulations, and then, following Bondi et al. (2008), fit an envelope of the form $S_{\text{TOT}} / S_{\text{PEAK}} = 1 + A(S/N)^B$ to the resulting source catalog, where S_{TOT} is the total flux density of a source and S_{PEAK} is its peak flux density. For point sources, $S_{\text{TOT}} = S_{\text{PEAK}}$, whereas for resolved sources $S_{\text{TOT}} > S_{\text{PEAK}}$. We find that the coefficients $A = 2.7$ and $B = -9.8$ define an upper limit above which fewer than 1% of our point-source models are artificially scattered due to noise (see Appendix A.2 for details), and hence apply this envelope as a quality control on the real data. The 15 SMGs with measured angular sizes in Table 1 all lie above this envelope, and have a median angular size of $\theta_{6\text{ GHz}} = 0''.53 \pm 0''.07$. Of these 15 SMGs with reliable sizes at 6 GHz, 9 are also spatially resolved (at $>3\sigma$) in our $870\text{ }\mu\text{m}$ dust continuum maps. The median FWHM sizes of these nine SMGs are $\theta_{6\text{ GHz}} = 0''.58 \pm 0''.10$ and $\theta_{870\text{ }\mu\text{m}} = 0''.49 \pm 0''.06$, a modest factor of $\sim 1.19 \pm 0.25$ (i.e., $\sim 1\sigma$) difference, corresponding to linear scales of $4.9 \pm 0.8\text{ kpc}$ and $4.1 \pm 0.4\text{ kpc}$, respectively. These 6 GHz sizes are comparable to the radio sizes measured recently at 3 GHz by Miettinen et al. (2017) in their study of SMGs in the COSMOS field (selected across a similar redshift range).

At 1.4 GHz, we find that 16/41 SMGs are reported as marginally resolved by IMFIT (with sizes measured to $>3\sigma$ significance), with a median deconvolved angular size of $\theta_{1.4\text{ GHz}} = 1''.35 \pm 0''.08$, corresponding to a linear scale of $10.9 \pm 0.1\text{ kpc}$. Of these 16 SMGs, 5 also have both 6 GHz and $870\text{ }\mu\text{m}$ sizes—the median 1.4 GHz deconvolved size of

this subsample is $\theta_{1.4\text{ GHz}} = 1''.35 \pm 0''.20$, $\sim 2.5 \pm 0.4$ times their $870\text{ }\mu\text{m}$ sizes.

We report these size measurements in Table 1. At each observing frequency, there are a number of SMGs for which we cannot measure reliable deconvolved sizes from IMFIT, which likely includes a combination of unresolved sources and sources for which a robust Gaussian fit cannot be obtained due to low S/N. To mitigate this bias, and to better understand the typical dust and radio continuum sizes of our 6 GHz-selected SMG sample, we also measure sizes in each of the stacked subsamples presented in Section 3.2. We find that the stacks of all 41 6 GHz-detected SMGs have deconvolved FWHM sizes of $\theta_{870\text{ }\mu\text{m}} = 0''.28 \pm 0''.06$, $\theta_{6\text{ GHz}} = 0''.54 \pm 0''.04$ ($\theta_{6\text{ GHz}}/\theta_{870\text{ }\mu\text{m}} \sim 1.8 \pm 0.4$) and $\theta_{1.4\text{ GHz}} = 1''.36 \pm 0''.16$ ($\theta_{1.4\text{ GHz}}/\theta_{6\text{ GHz}} \sim 2.6 \pm 0.4$). We also report the deconvolved sizes of the bright, faint, and convex stacks in Table 1.

4. Discussion

4.1. Modeling the Radio Spectra of SMGs

A significant finding of our work is that a subsample (10/41) of our 6 GHz-detected SMGs exhibit radio spectra that steepen at higher frequency, in contrast with local ULIRGs (Condon 1992) and $\sim\mu\text{Jy}$ high-redshift star-forming galaxies (Murphy et al. 2017) that exhibit flattening spectra toward higher frequency. We now investigate this phenomenon within the context of a model that takes into account cooling timescales for CREs. In general, the cooling timescale of CREs at an energy $E = h\nu_C$ is $\tau_{\text{cool}}^{-1} = \tau_{\text{IC}}^{-1} + \tau_{\text{sync}}^{-1} + \tau_{\text{brem}}^{-1} + \tau_{\text{ion}}^{-1}$, with energy losses due to inverse Compton, synchrotron, bremsstrahlung, and ionization processes, respectively. In each of these processes, higher energy electrons (which produce higher frequency synchrotron emission) lose their energy more rapidly than lower energy electrons (whose emission dominates the synchrotron spectrum at lower frequencies), such that, over time, the aging radio spectrum builds up a “break” at frequency ν_C (known as the “critical frequency”), which moves to successively lower frequency as the CRE population ages (Carilli & Barthel 1996). Thompson et al. (2006) and Murphy et al. (2008) give approximate forms for these cooling timescales as a function of the critical frequency and properties of the host galaxy:

$$\left(\frac{\tau_{\text{IC}}}{\text{yr}}\right) \sim 5.7 \times 10^7 \left(\frac{\nu_C}{\text{GHz}}\right)^{-1/2} \left(\frac{B}{\mu\text{G}}\right)^{1/2} \left(\frac{10^{-12}\text{ erg cm}^{-3}}{U_{\text{rad}}}\right) \quad (3)$$

$$\left(\frac{\tau_{\text{sync}}}{\text{yr}}\right) \sim 1.4 \times 10^9 \left(\frac{\nu_C}{\text{GHz}}\right)^{-1/2} \left(\frac{B}{\mu\text{G}}\right)^{-3/2} \quad (4)$$

$$\left(\frac{\tau_{\text{ion}}}{\text{yr}}\right) \sim 10^9 \left(\frac{n_{\text{H}}}{\text{cm}^{-3}}\right)^{-1} \left(\frac{\nu_C}{\text{GHz}}\right)^{1/2} \left(\frac{B}{\mu\text{G}}\right)^{-1/2} \quad (5)$$

$$\left(\frac{\tau_{\text{brem}}}{\text{yr}}\right) \sim 3 \times 10^7 \left(\frac{n_{\text{H}}}{\text{cm}^{-3}}\right)^{-1}. \quad (6)$$

We estimate the typical radiation field strengths of our SMGs, U_{rad} , from their rest frame 8–1000 μm luminosities (L_{IR}) measured in Section 3.3 via the relation $U_{\text{rad}} \propto L_{\text{IR}} / (2\pi R^2 c)$ for a disk radius R , where c is the speed of light.

The magnetic field strength, B , is estimated under the assumption of magnetic flux freezing as used by Miettinen et al. (2017), i.e., $B \approx 10\text{ }\mu\text{G} \times \sqrt{n_{\text{H}}/\text{cm}^{-3}}$. n_{H} is the hydrogen gas density, which we estimate from the dust masses obtained via far-IR SED fitting (Section 3.3), and using an integrated gas-to-dust ratio $\delta_{\text{GDR}} = 100$ that is appropriate for

SMGs (Swinbank et al. 2014). We begin with the assumption that the majority of the cold gas in our SMG sample is located in disks whose radii are comparable to the typical $^{12}\text{CO } J=1-0$ sizes of SMGs, i.e., $R \sim 8-10$ kpc (Ivison et al. 2011; Thomson et al. 2012), with a putative vertical scale height $h \sim 1$ kpc. The typical gas density is therefore approximately $n_{\text{H}} = (M_{\text{dust}} \times \delta_{\text{GDR}}) / (\pi R^2 h) \sim 12 \pm 2 \text{ cm}^{-3}$, yielding $B \sim 35 \pm 3 \mu\text{G}$.²²

The typical radiation field strength within the region traced by the dust is $U_{\text{rad}} \propto L_{\text{IR}} / R_{\text{dust}}^2 \sim (1.5 \pm 0.4) \times 10^{-9} \text{ erg s}^{-1} \text{ cm}^{-2}$. However, under the flux-freezing assumption discussed above, the magnetic field—which defines the “bath” in which CREs lose their energy—is traced by the gas disk, with a radius R_{gas} , which may be up to $5\times$ larger than that of the dust disk. Throughout this larger region, the average radiation field strength is an order of magnitude weaker, $U_{\text{rad}} \propto L_{\text{IR}} / R_{\text{gas}}^2 \sim (1.2 \pm 0.3) \times 10^{-10} \text{ erg s}^{-1} \text{ cm}^{-2}$.

Together, these two extreme estimates of the radiation field strength imply cooling timescales $\tau_{\text{cool}} \sim 10^4-10^5$ yr for the emission probed by our observed frame 6 GHz observations. At the relatively modest B -field strengths implied by the flux-freezing assumption, this timescale is determined by dominant synchrotron losses. These cooling timescales are similar to those estimated by Miettinen et al. (2017) for their sample of SMGs in COSMOS.

The unexpected steepening of the radio spectra at higher frequency seen in a subset of our sample (Figure 2) implies either a severe steepening of the synchrotron emission at higher frequencies (an effect that is then mitigated by the addition of a strong, flatter spectrum free-free component), or that the free-free component is suppressed (or absent), in which case the observed spectral curvature can be explained by more modest synchrotron steepening.

We explore these possibilities by constructing a model for the evolution of the synchrotron spectra of our galaxies. In nearby radio galaxies, there is a well-established relationship between the steepness of the radio spectrum and the age of the radio emission. If synchrotron emission is injected into the ISM via an instantaneous event (e.g., a single Type II supernova (SN)), with a power-law injection index $\alpha_{\text{inj}} = -0.8$ out to infinite frequency, then as the spectrum ages, high-energy electrons will, as previously discussed, lose energy (via a combination of inverse Compton, synchrotron, ionization, and bremsstrahlung processes) more rapidly than low-energy electrons, resulting in losses of radio power that are more severe at higher frequencies. This naturally produces a steepening of the radio spectrum above a critical frequency, ν_{C} , and is the means by which the ages of synchrotron jets in powerful AGN are determined (e.g., Carilli & Barthel 1996). For synchrotron losses, after a time t_{sync} , the critical frequency is

$$\left(\frac{\nu_{\text{C}}}{\text{GHz}} \right) = 1610^2 \left(\frac{B}{\mu\text{G}} \right)^{-3} \left(\frac{t_{\text{sync}}}{\text{Myr}} \right)^{-2}. \quad (7)$$

Assuming no pitch-angle scattering of relativistic particles, then for $\nu < \nu_{\text{C}}$, the low-frequency spectral index, α_{L} , remains unchanged from the injection spectral index, while at $\nu > \nu_{\text{C}}$, the high-frequency spectral index, α_{H} is steepened to $\alpha_{\text{H}} = (4/3)\alpha_{\text{L}} - 1$ (the Kardashev–Pacholczyk model; Kardashev 1962; Pacholczyk 1970). Thus, for an instantaneous injection of

synchrotron-emitting electrons observed at time t_{sync} (Myr), the low-frequency spectral index is expected to remain the same as the original injection spectrum ($\alpha_{\text{L}} = -0.8$), while the spectral index at frequencies higher than the critical frequency becomes $\alpha_{\text{H}} = -2.1$.

Of course, the radio spectra of star-forming galaxies are not the product of instantaneous injection events, but instead reflect the aggregate of the synchrotron emission produced throughout the star formation history of the host galaxy (minus the aforementioned age/frequency dependent losses), plus the flatter spectrum thermal free-free component tracing current star formation.

Clearly, detailed modeling of this interplay between ongoing synchrotron injection and aging processes in distant starburst galaxies is beyond the scope of this work, however we can begin to investigate these processes by de-redshifting the radio spectrum of our convex subsample of SMGs and fitting the resulting rest-frame radio spectrum using a simple model for synchrotron losses. We begin by using the median far-IR luminosity of the convex sample to estimate a representative $\text{SFR}_{\text{convex}} = (850 \pm 120) M_{\odot} \text{ yr}^{-1}$, and convert this to an expected free-free luminosity density (at $\nu_{\text{rest}} = 20$ GHz) of $L_{\text{FF}} = (1.3 \pm 0.1) \times 10^{23} \text{ W Hz}^{-1}$ using the relations in Murphy et al. (2011). Given a free-free spectral index of $\alpha_{\text{FF}} = -0.1$, this allows us to estimate the thermal contribution to the rest-frame radio SED as a function of frequency, and subtract it to obtain a pure synchrotron spectrum.

We then model the evolution in the shape of this synchrotron spectrum throughout a 100 Myr constant SFR episode (i.e., a “top hat” star formation history) by generating a grid of broken power laws from $\nu_{\text{rest}} = 0.1-40$ GHz (arbitrarily normalized in flux at 100 MHz) using Equation (7) for instantaneous synchrotron ages $t_i = 0-200$ Myr and magnetic fields that vary from $B = 1-100 \mu\text{G}$, and summing these aged “instantaneous burst” synchrotron spectra for an ongoing starburst event “observed” at times $t_{\text{obs}} = (200 - t_i)$ Myr following the onset of star formation.

As t_{obs} increases, so does the age of the oldest synchrotron component present in the model spectrum (t_{sync}), thus leading to a steepening of the spectral index at higher frequency. Due to inverse Compton losses off the strong radiation field produced by the (ongoing) star formation, a fraction ($f(t) \propto \text{SFR}(t)$) of this previously injected/aged emission is suppressed at each time step. As noted previously, inverse Compton losses are also a function of frequency and B -field strength, however our three-band radio photometry do not provide sufficient constraints to simultaneously model two-frequency and B -field-dependent processes. We therefore impose the simplifying constraint that inverse Compton losses (which are subdominant to synchrotron losses over the range of B -fields and U_{rad} estimated for our SMG sample) result in an additional frequency-independent suppression in the total radio power of $\sim 5\%/\text{Myr}$ (e.g., Schleicher & Beck 2013). We note that more detailed modeling of inverse Compton losses as a function of frequency would likely change the derived synchrotron ages, but not the general behavior of the synchrotron aging model.

Hence in our model, at any time t_{obs} during an ongoing episode of star formation, the synchrotron spectrum $\zeta_{\text{sync}}(\nu, t_{\text{obs}})$ can be described as

$$\zeta_{\text{sync}}(\nu, t_{\text{obs}}) = \sum_{i < t_{\text{obs}}} (1 - f_i) \times \zeta_{\text{sync}}(\nu, t_i) + \rho(t_{\text{obs}}) \times \zeta_{\text{sync}}(t_{\text{obs}}), \quad (8)$$

where $\zeta_{\text{sync}}(\nu, t_i)$ are the individual synchrotron components in the ISM arising from injection at all prior time steps, $t_i < t_{\text{obs}}$, $f \equiv 0.05$ is the aforementioned damping coefficient that

²² Here, the uncertainty on the magnetic field strength is purely statistical, arising from the uncertainty on the dust mass, and does not account for the inherent systematic uncertainties entailed in the choice of dust-to-gas ratio, gas disk volume, or the assumption of flux freezing.

accounts for inverse Compton losses off the local radiation field, and $\rho(t_{\text{obs}})$ is a multiplicative factor that scales the amount of emission injected at each t -step relative to the star formation history. In the simple case of a 100 Myr long top hat star formation history (wherein the SFR is constant from 0–100 Myr and then terminates), $\rho = 1$ and f is a constant.²³

Finally, the model synchrotron spectrum arising from this sum (which is arbitrarily scaled, but has a spectral shape that is uniquely determined by the combination of t_{obs} , magnetic field strength, and star formation history) is normalized to match the observed radio fluxes in the three bands.

We emphasize that the arbitrary re-normalization of this model to fit the data at each time step means that it is not able to capture in detail the multitude of processes by which synchrotron emission is injected into and attenuated within the ISM, however our toy model can track the dependency of the (galaxy-integrated) radio spectral *shape* as a function of age and magnetic field strength, allowing us to determine which (if any) combination of t_{sync} and magnetic field strength can reproduce the observed spectral break in our SMG composite SED.

Examples of how the rest-frame SED shape evolves (for a constant SFR and fixed magnetic field strength $B = 35 \mu\text{G}$, as estimated via the flux-freezing assumption) are shown in Figure 5. For the typical ISM conditions of our SMGs, we find that a synchrotron age $t_{\text{sync}} \sim 35 \pm 10$ Myr reproduces the observed spectral break. We stress that t_{sync} corresponds to the time that has elapsed since synchrotron emission first appeared in the radio spectrum of a galaxy, and is not, in general, synonymous with the age of the current starburst. We will return to this point in Section 4.3.

4.2. The Multifrequency Sizes of SMGs

Recently, Miettinen et al. (2017) measured the 3 GHz FWHM sizes for a sample of SMGs selected at $1100 \mu\text{m}$ in the COSMOS field, finding a median $\theta_{3 \text{ GHz}} = 4.6 \pm 0.4$ kpc, a factor $\sim 1.9 \pm 0.2$ larger than the $870 \mu\text{m}$ dust continuum sizes measured for the AS2UDS SMGs studied here by Simpson et al. (2015) and Stach et al. (2019). Using estimates of the cooling times for CREs, Miettinen et al. (2017) argued that this apparent mismatch in the spatial scales traced by radio/submillimeter emission in SMGs cannot be due to transport of CREs produced in the dusty nuclear starburst to the outer disk region, as—given typical ISM conditions—the CRE cooling times are too short (by orders of magnitude) to allow propagation on the required scales.

The maximum distance (l_{cool}) that CREs can propagate before cooling is given as $l_{\text{cool}} = (D_E \tau_{\text{cool}})^{1/2}$, where D_E is the diffusion coefficient. Following Murphy et al. (2008), we use the piecewise empirical CRE diffusion coefficient measured by Dahlem et al. (1995) in the local starburst galaxies, NGC 891 and NGC 4631:

$$\left(\frac{D_E}{\text{cm}^2 \text{ s}^{-1}} \right) \sim \begin{cases} 5 \times 10^{28}, & E < 1 \text{ GeV} \\ 5 \times 10^{28} \left(\frac{E}{\text{GeV}} \right)^{1/2}, & E \geq 1 \text{ GeV}. \end{cases} \quad (9)$$

²³ For more complicated star formation histories, $\rho(t) \propto 1/f(t)$, since a higher (lower) SFR implies a higher (lower) radiation field strength, which implies more (less) rapid inverse Compton losses of the preexisting radio emission in the galaxy at time t .

Thus,

$$\left(\frac{l_{\text{cool}}}{\text{kpc}} \right) \sim 7 \times 10^{-4} \left(\frac{\tau_{\text{cool}}}{\text{yr}} \right)^{1/2} \left(\frac{\nu_C}{\text{GHz}} \right)^{1/8} \left(\frac{B}{\mu\text{G}} \right)^{-1/8}. \quad (10)$$

For the combination of t_{cool} and magnetic field strength estimated above, and with D_E from Dahlem et al. (1995), we find that CREs whose energies produce $\nu_{\text{rest}} \sim 20$ GHz radio emission have $l_{\text{cool}} \sim 100\text{--}400$ pc. The 6 GHz radio FWHM of our stacked SMGs is $\sim 1.9 \pm 0.4 \times$ (or $2\text{--}3$ kpc) larger than the $870 \mu\text{m}$ dust sizes. Given the rapid cooling timescales described above, we therefore concur with Miettinen et al. (2017) that diffusion of CREs from a nuclear starburst traced by the dust emission is an unlikely explanation for the enlarged radio sizes of SMGs relative to their dust sizes, unless the CRE diffusion coefficient D_E in SMGs is almost three times as large as that measured empirically in local starbursts by Dahlem et al. (1995). We will return to this in Section 4.3.

Comparing our new multifrequency radio/submillimeter observations of bright SMGs to observations of ionized/molecular gas in SMGs from the literature, we see an apparent trend whereby SMGs have larger physical sizes at lower observed continuum frequencies, and that these larger low-frequency continuum sizes successively better trace the full extent of their diffuse ISM. To summarize, the typical FWHM of the $870 \mu\text{m}$ (rest frame $\sim 250 \mu\text{m}$) cold dust emission in SMGs is $\sim 0''.3$ ($r_d \sim 2\text{--}3$ kpc), while the 6 GHz (rest frame ~ 20 GHz) radio sizes are $\sim 0''.5$ ($r_{6 \text{ GHz}} \sim 4\text{--}6$ kpc). At 1.4 GHz (rest frame ~ 5 GHz), a subset of our SMGs are spatially resolved on $\sim 1''.3$ ($r_{1.4 \text{ GHz}} \sim 10$ kpc) scales, in good agreement both with previously measured 1.4 GHz SMG sizes in the Lockman Hole field obtained with high-resolution ($\sim 0''.2$) Multi-Element Radio-Linked Interferometer Network (MERLIN) imaging (Biggs & Ivison 2008), and with the stellar disk sizes of SMGs in the ECDFS field measured via near-IR imaging with *HST* (Aguirre et al. 2013; Chen et al. 2015). Moreover, observations of cold gas tracers in SMGs show the ISM of SMGs to be extended on scales of $\gtrsim 10$ kpc (Ivison et al. 2011; Thomson et al. 2012; Emonts et al. 2016; Dannerbauer et al. 2017; Gullberg et al. 2018).

In a recent study, Chen et al. (2017) measured the $^{12}\text{CO } J = 3\text{--}2$, stellar light, $\text{H}\alpha$ and $870 \mu\text{m}$ dust continuum sizes of the SMG ALESS 67.1, finding similar size discrepancies to those quoted above *within the same galaxy*, indicating that these trends and are not simply driven by biases in the individual samples used to infer them.

Throughout this paper, we have interpreted our results within the context of a model in which the “typical” SMG is comprised of a compact, dusty starburst—traced by the $870 \mu\text{m}$ emission—which acts as the source of the galaxy’s primary CREs. CREs produced by a nuclear starburst are unable to propagate far from the regions in which they were injected into the ISM (due to their short lifetimes), however cosmic-ray nuclei (CRNs) may plausibly propagate outward into the more extended, quiescent gas disk (e.g., Strong & Moskalenko 1998), where they would release their energy via spallations with the baryonic content of the ISM, triggering a cascade of secondary CREs and second-generation synchrotron emission. If a large proportion of CRNs propagate and spallate in this manner, then the buildup of a low-frequency radio “halo” extending beyond the nuclear starburst may be expected. Because the rate of CRN/CRE production is proportional to the SFR (e.g., Papadopoulos et al. 2011), as is the rate of dust-heating, both

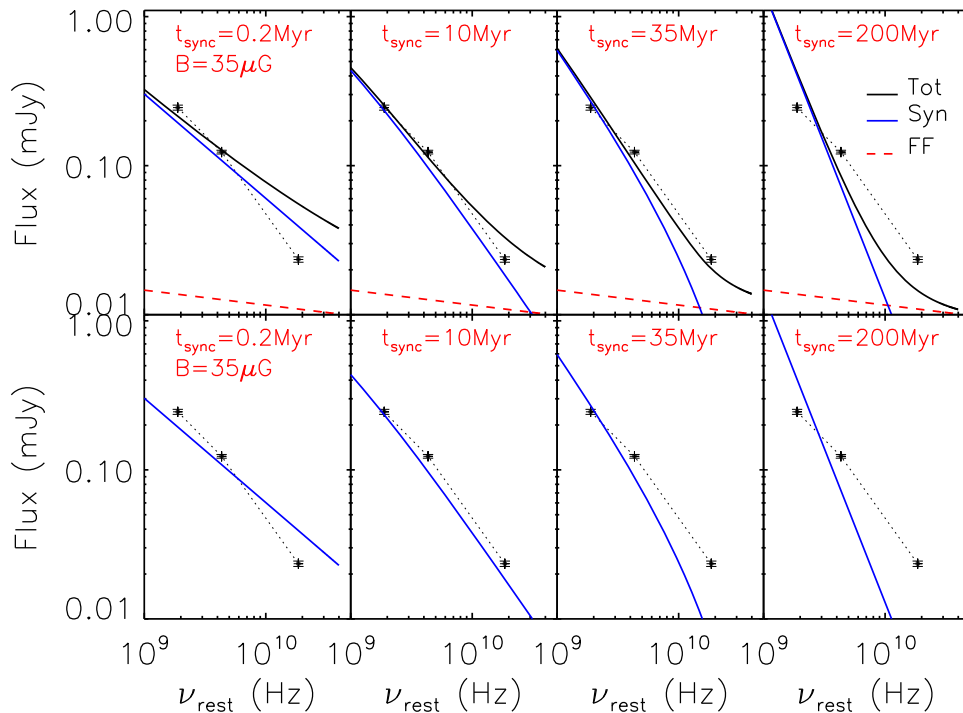


Figure 5. The rest-frame composite SED of our 6 GHz-selected SMG sample, along with fitted radio spectra produced by the simple model for synchrotron aging outlined in Section 4.1. Top row, left to right: Example SEDs at four different ages, in which the strength of the free-free component is estimated from L_{IR} under the condition that $\text{SFR}_{\text{IR}} = \text{SFR}_{\text{FF}}$, and using the luminosity-to-SFR relationships of Murphy et al. (2011) to subtract the appropriate free-free contribution to the radio flux densities. The synchrotron model is generated as described in Section 4.1, and the total model SED is the sum of the synchrotron and free-free components. At early times ($t_{\text{sync}} < 1$ Myr), the synchrotron spectrum has a constant power-law form (with $\alpha_L = \alpha_H = 0.8$) from $\nu_{\text{rest}} \sim 1$ –100 GHz which, when added to the free-free component, results in a modest flattening of the SED toward higher frequencies. As the starburst ages, a break in the synchrotron component gradually appears above a critical frequency, ν_C , as described by Equation (7). By $t_{\text{sync}} = 10$ Myr, the ISM contains a mixture of synchrotron components with ages $0 \text{ Myr} < t_{\text{sync}} < 10 \text{ Myr}$ (in a proportion that is determined by the assumed star formation history), and thus the (severe) spectral steepening that has already begun to affect the oldest component(s) does not dominate the integrated SED. After the starburst terminates, there is no mechanism to inject new high-frequency emission to mitigate the (rapid) losses due to spectral aging of previously injected components, and the spectral index is rapidly steepened to $\alpha \sim -2.1$. For a $B = 35 \mu\text{G}$ magnetic field, the optimal fit is achieved at $t_{\text{sync}} \sim 35$ Myr. Bottom row, left to right: As per the top row, except with the free-free component totally suppressed (as in Arp 220; see Barcos-Muñoz et al. 2015, and Appendix A.3), which implies that the radio emission is dominated at all frequencies by the synchrotron component. For a given B -field, with no free-free component to mitigate the spectral steepening caused by the aged-synchrotron component, the best-fitting synchrotron age is typically lowered by ~ 5 –15 Myr (see Appendix A.3).

the total radio and total far-IR luminosities would share a common origin, and thus the far-IR/radio correlation would hold on a galaxy-averaged sense. However, any mismatch between the typical dust and ^{12}CO spatial extents in SMGs in this model would require there to be a (local) breakdown in the Kennicutt–Schmidt law, due to the implied presence of high-surface density molecular gas on the outskirts of this nuclear starburst that is not co-located with the current star formation, traced by the submillimeter emission. We will return to this idea of CRN propagation in Section 4.3.

Alternatively, the mismatch in dust and radio continuum sizes in SMGs may be because the dust sizes themselves do not trace the full extent of the current star formation. Dust may be driven from the central regions of a starburst galaxy either via direct photon pressure (e.g., Nath et al. 2012) or by being swept up in CR outflows (e.g., Tatischeff & Kiener 2004; Uhlig et al. 2012) that propagate along magnetic field lines and terminate at large radii. Because the surface brightness sensitivity of an interferometer is inversely proportional to the angular resolution, dispersing a large fraction of dust from the nuclear starburst to a more diffuse structure could—paradoxically—make the dust appear more compact in ALMA $870 \mu\text{m}$ continuum imaging, as it would shrink the region of the dust reservoir that is of sufficient surface brightness to be detectable in any given observation.

To search for signs of undetected, extended low surface brightness cold dust emission, we performed a uv stack of the ALMA $870 \mu\text{m}$ continuum data for all 716 SMGs in the UDS field. The rms of our stacked ALMA image is $\sigma_{870 \mu\text{m}} \sim 29 \mu\text{Jy beam}^{-1}$, a factor $\sim 30\times$ deeper than that of a single snapshot image. In the stacked image, we do see evidence of a weak, extended dust component on $\sim 1''$ scales, however this accounts for only $\sim 1\%$ of the total $870 \mu\text{m}$ flux density. Hence we argue there is no compelling evidence for a significant mass of previously unseen diffuse, cold dust that could enshroud a large amount of star formation, and explain the radio/submillimeter size mismatch.

To summarize, we believe the large 1.4 GHz sizes of our SMGs (relative to their dust sizes) are most likely due to the radio emission being distributed on scales beyond those on which the bulk of the (current) star formation is occurring, and that higher frequency radio sizes provide a more accurate tracer of the current nuclear starburst.

4.3. Cosmic-Ray Propagation and the Age of the Starburst

In Section 4.1, we determined the combinations of magnetic field strength (B) and synchrotron age (t_{sync}) that best fit the observed composite radio SED for our convex SMG sample. To convert these synchrotron ages to t_{SB} , the time elapsed since

the onset of the current starburst phase, it is necessary to consider possible time lags inherent in the model.

One contribution to the time lag, Δt_{SNe} , occurs simply because the primary population of CREs, which produce synchrotron emission is built up due to SN explosions, which occur $\sim 10\text{--}20$ Myr after the onset of the starburst (i.e., the typical lifetimes of OB stars).

A second time lag, Δt_{CR} , may occur if the transport time of cosmic rays to the regions of the ISM in which they lose their energy (i.e., produce their synchrotron emission) is non-negligible. Primary CRs produced in SNe comprise a mixture of relativistic antiprotons, electrons, positrons, and nucleons (e.g., Grenier et al. 2015), however the bulk of the synchrotron emission observed in the radio continuum is believed to originate from energy losses of short-lived CREs and positrons off the magnetic field of the host galaxy. We have already shown that barring an unusually high diffusion coefficient, propagation of primary CREs from the nuclear starburst is unlikely to explain the radio/far-IR size mismatch. However, the energy loss of primary CRNs (themselves produced via SNe) is thought to be a more complicated, multichannel process, in which the spallations of CRNs on the baryonic content of the ISM produces a cascade of secondary cosmic rays, and thus the ingredients required for secondary synchrotron emission (Strong et al. 2007; Zweibel 2013).

In a study of the effect of cosmic-ray streaming in hydrodynamical simulations of galaxy formation, Uhlig et al. (2012) found that cosmic rays produced by a compact nuclear starburst can be blown out into the ISM in a wind, which produces Alfvén waves as it interacts with the galaxy magnetic field. While individual cosmic rays move at close to the speed of light along spiral trajectories shaped by magnetic field lines, the Alfvén waves they produce as they do so act as a brake on the cosmic-ray bulk speed, with the energy and momentum carried by the cosmic-ray population being transferred to the thermal gas. This momentum transfer produces instabilities in the gas disk, which re-excite the Alfvén waves further limiting cosmic-ray streaming. Thus, the transfer of energy and momentum from cosmic rays to the ISM is a self-throttling process.

In their multifrequency radio study of the nearby starburst galaxy NGC 253, Heesen et al. (2009) approximated the typical cosmic-ray bulk speed as $v_{\text{CR}} \sim v_{\text{W}} + v_{\text{A}}$, where $v_{\text{A}} = B/\sqrt{4\pi\rho}$ is the Alfvén speed and v_{W} is the observed outflow speed of the thermal gas. Without spectrally and spatially resolved observations of the molecular ISM in our SMG sample, we cannot determine v_{W} directly; however work by Banerji et al. (2011), George et al. (2014), and Riechers et al. (2014) has found representative outflow velocities (via [O II], OH, and [C II] line emissions, respectively) of $v_{\text{W}} \sim 100\text{--}500 \text{ km s}^{-1}$ in starbursting SMGs. Given the estimated magnetic field strengths and gas densities for our SMG sample (Table 2), we estimate a typical $v_{\text{A}} \sim 1200 \text{ km s}^{-1}$, and hence $v_{\text{CR}} \sim 1500 \text{ km s}^{-1}$.

If propagation and spallation of CRNs from the central, dusty starburst is the primary explanation for the $\sim 5\text{--}8$ kpc mismatch in scale between the dust and 1.4 GHz radio continuum sizes, then the implied CR propagation timescale is $\Delta t_{\text{CR}} \sim 5$ Myr. Thus, an approximate age for the starburst can be deduced from the best-fitting synchrotron age as $t_{\text{SB}} \sim t_{\text{sync}} + \Delta t_{\text{SNe}} + \Delta t_{\text{CR}}$. We show contours of starburst age (t_{SB}) versus magnetic field strength for our best-fitting

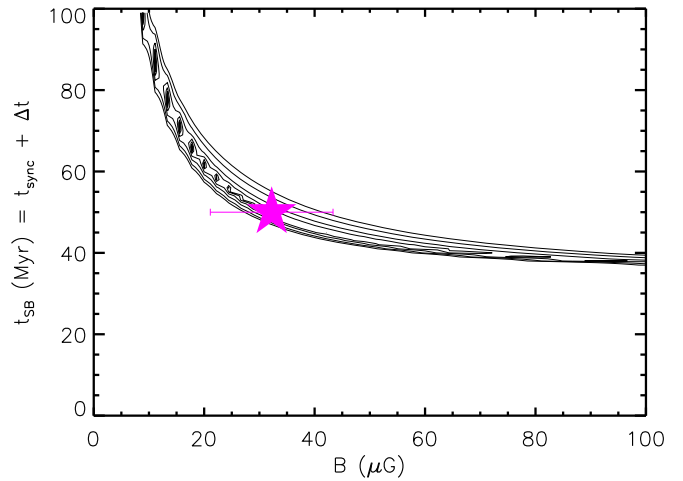


Figure 6. χ^2 contours for our model radio SEDs as a function of B and t . The contours begin at $\chi^2 = \chi^2_{\text{min}} + 1$, and increase in steps of $\chi^2_n = 2 \times \chi^2_{n-1}$ thereafter. The statistical uncertainty on the median magnetic field strength of our SMG sample is $\Delta B \sim 2 \mu\text{G}$ (Section 4.1). As our model for the spectral shape has only one free parameter (B), the $\pm 1\sigma$ confidence interval on the best-fitting t is equal to the spacing of the innermost pair of contours at the corresponding value of B (i.e., $\pm \Delta \chi^2 = 1$). The statistical uncertainties on t and B are thus too small to be plotted, but we reiterate that these do not account for model-dependent systematics. Note that the ordinate is the starburst age, $t_{\text{SB}} = t_{\text{sync}} + \Delta t$, where $\Delta t \sim 25$ Myr accounts for the time lags between the onset of star formation and the production of the observed synchrotron emission. In Section 4.3, we discuss possible contributions to Δt , including: (i) the time lag between the onset of the current starburst and the production of the first SNe, which arises after the lifetime of a typical OB star ($\sim 10\text{--}20$ Myr); (ii) the travel time of cosmic-ray nucleons from the starburst to the regions of the ISM in which they lose their energy (determined by the cosmic-ray wind speed) and produce synchrotron emission. Our best estimate for the magnetic field strength is $B \sim 35 \mu\text{G}$, which implies a starburst age $t_{\text{SB}} \sim 50 \pm 10$ Myr.

synchrotron model with these offsets applied in Figure 6. We see that, for an estimated magnetic field strength $B = 35 \mu\text{G}$, the best-fit starburst age (including time lags) is $t_{\text{SB}} \sim 50 \pm 10$ Myr, but note that this magnetic field strength depends on the assumption of flux freezing, and is proportional to the gas density ($B \propto \sqrt{n_{\text{H}}}$), which we have constrained only loosely via the measured dust masses. However, even allowing for a factor $4\times$ increase(decrease) in n_{H} would only increase (lower) the magnetic field strength by a factor $2\times$. From Figure 6, we see that for $B \sim 15\text{--}60 \mu\text{G}$, $t_{\text{SB}} \sim 40\text{--}80$ Myr, and thus our estimates of the synchrotron ages of our 6 GHz SMG sample are not strongly dependent upon our assumptions for the gas disk size and morphology.

Based on the far-IR SED fits to the 99 SMGs observed in the ECDFS field (the ALESS sample), Swinbank et al. (2014) used measurements of the SFR (obtained via L_{IR}) and gas mass (obtained via the dust masses and a gas-to-dust ratio) to infer typical gas depletion timescales for SMGs of $\tau_{\text{dep}} \sim 130$ Myr (see also Bothwell et al. 2013). This is consistent with crude estimates of the lifetimes of SMGs obtained via clustering analyses (e.g., Hickox et al. 2012). From our model we find that a spectral break strong enough to be detectable in our radio observations ($\alpha_{610 \text{ MHz}}^{1.4 \text{ GHz}} - \alpha_{1.4 \text{ GHz}}^{6 \text{ GHz}} \gtrsim 0.3$) is seen $\sim 40\text{--}80$ Myr into the star formation event. The fact that we see such features in $\sim 25\%$ of our sample suggests that the total duration of the submillimeter-bright starburst phase is thus likely to be $\sim 100\text{--}150$ Myr, with those sources that display strong spectral breaks being on average at an earlier phase in their ongoing evolution than the remainder of the sample.

5. Conclusions

We have studied the radio and rest-frame far-IR properties of a sample of 41 6 GHz-detected submillimeter-selected galaxies from the AS2UDS survey. Combining high-resolution ($0''.3$) ALMA 870 μm imaging with radio imaging at 6 GHz (probing $\nu_{\text{rest}} \sim 20$ GHz) at comparable resolution from the VLA, we investigate the spectral shape and relative scales of the dust and radio emission.

1. We find that the spectral indices of radio-bright SMGs steepen toward higher frequencies in a subset of $\sim 25\%$ our sample (from $\langle \alpha_{610\text{ GHz}}^{1.4\text{ GHz}} \rangle = -0.60 \pm 0.06$ to $\langle \alpha_{1.4\text{ GHz}}^{6\text{ GHz}} \rangle = -1.06 \pm 0.04$), defying simple models for the radio emission in star-forming galaxies that predict that radio SEDs should become successively flatter at higher frequencies due to an increasing free-free component. We have investigated the possibility that our 6 GHz flux densities are spuriously low, but find no evidence for this—we therefore conclude that the convex spectral behavior seen in $\sim 25\%$ of our SMGs reflects their uniquely high SFR surface densities, relative to the low-SFR, μJy radio population at high redshift (Murphy et al. 2017). Our observations suggest that either synchrotron or free-free emission (or possibly both) are suppressed at high frequencies in the extreme environments of SMGs.
2. We develop a simple model for the radio emission in bright SMGs in which the observed spectral curvature arises due to aged-synchrotron emission in the presence of an ongoing episode of intense star formation. We use the gas masses of our SMG sample (derived from their dust masses via a gas-to-dust ratio that is appropriate for SMGs) to infer their magnetic field strengths, from which our model predicts magnetic field strengths of $B \sim 35 \mu\text{G}$ and synchrotron ages $t_{\text{sync}} \sim 35 \pm 10$ Myr. Accounting for the time lags between the onset of star formation and (i) the production of the first SNe and (ii) the propagation of cosmic-ray nucleons to $\sim\text{kpc}$ radii in the gas disk (where they release their energy via interactions with the ISM, producing secondary cosmic-ray electrons, and thus additional synchrotron emission), we find that these synchrotrons' ages correspond to starburst ages of $t_{\text{SB}} \sim 40\text{--}80$ Myr. These ages are consistent with estimates of the expected lifetimes of SMGs from other observations.
3. We find that the (deconvolved) 6 GHz radio size of our stacked SMG sample is $(\sim 1.8 \pm 0.4) \times$ more extended than the stacked 870 μm dust emission ($\theta_{6\text{ GHz}} = 0''.51 \pm 0''.05$, see $\theta_{6\text{ GHz}} = 0''.28 \pm 0''.06$), while at least a subset of our sources are spatially resolved at 1.4 GHz, at which they are $\sim 2.5 \times$ larger still ($\theta_{1.4\text{ GHz}} = 1''.34 \pm 0''.18$). We posit that this size mismatch may be consistent with the production of low-energy secondary CREs in the gas disk, far from the nuclear starburst, due to the interaction of CRNs (produced by the starburst) and baryonic material in the circumnuclear region.

Local starburst galaxies such as NGC 253 and Arp 220 have cosmic-ray rates $\gtrsim 10^4 \times$ higher than the Milky Way (e.g., Meijerink et al. 2011). In such extreme cosmic-ray dominated regions (CRDRs), the minimum gas temperature may be elevated by as much as ~ 100 K, becoming thermally decoupled from the dust. At these temperatures, astrochemical models of CRDRs predict the efficient transmutation of ^{12}CO into atomic/ionized carbon, and hence of elevated [C I] and [C II] to low- J ^{12}CO line ratios (e.g., Bisbas et al. 2017). Hence, an important future test of

our model—which posits that the multifrequency radio sizes and source-integrated radio spectra of SMGs might be the result of transport and spallations of CRNs in the extended gas disk—will be to perform a resolution-matched spectral line survey of SMGs in order to search for radial variations in the $^{12}\text{CO}/[\text{C I}]$ and $^{12}\text{CO}/[\text{C II}]$ profiles of SMGs.

Disentangling the complex spectro-morphological properties of high-redshift starburst galaxies is challenging, given the capabilities of the current VLA (particularly, its lack of resolving power at low frequencies). However these results (both the convex source-integrated radio spectra and enlarged sizes at lower frequency relative to higher frequency) provide tantalizing evidence that the processes of cosmic-ray propagation—which dominate the spectral behavior of, and create low-frequency radio continuum halos around nearby starburst galaxies (e.g., Heesen et al. 2016; Mulcahy et al. 2018)—may also be at work (and be observable) in the environments of high-redshift starburst galaxies. Forthcoming instruments (such as Square Kilometre Array (SKA), and the proposed ngVLA) and deep imaging surveys being undertaken with existing longer-baseline interferometers (such as the *e*-MERLIN Galaxy Evolution survey, which maps the GOODS-N field at 1.4 GHz at $\sim 0''.3$ resolution down to $\sim \mu\text{Jy beam}^{-1}$ sensitivities; T. W. B. Muxlow et al. 2019, in preparation; Thomson et al. 2019) will provide the capabilities to create subarcsecond, resolution-matched spectral index maps of high-redshift galaxies. These will allow us to directly address this issue, yielding new constraints on the mechanisms powering the radio emission in starburst galaxies at high redshift.

We would like to thank the anonymous reviewer for their useful comments, which greatly improved the content and presentation of this paper. A.P.T., I.R.S., E.A.C., and B.G. acknowledge support from the ERC Advanced Grant DUSTYGAL (# 321334). A.P.T., I. R.S., E.A.C., A.M.S., B.G., and J.L.W. acknowledge STFC (ST/P000541/1). A.P.T. is immeasurably grateful to David Rosario, Rob Ivison, Eva Schinnerer, Rob Beswick, Tom Muxlow, and Todd Thompson who have all provided helpful advice and insight throughout the preparation of this manuscript. I.R.S. also acknowledges support from a Royal Society Wolfson Merit Award. E.I. acknowledges partial support from FONDECYT through grant No. 1171710. W.R. is supported by the Thailand Research Fund/Office of the Higher Education Commission grant No. MRG6080294 and Chulalongkorn University's CUniverse. M.J.M. acknowledges the support of the National Science Centre, Poland, through the POLONEZ grant 2015/19/P/ST9/04010; this project has received funding from the European Union's Horizon 2020 research and innovation programme under the Marie Skłodowska-Curie grant agreement No. 665778. We gratefully acknowledge funding toward the VLA 3-bit samplers used in this work from ERC Advanced Grant 321302, COSMICISM. J.L.W. acknowledges support from a European Union COFUND/Durham Junior Research Fellowship (EU grant agreement No. 609412) and an STFC Ernest Rutherford Fellowship (ST/P004784/1 and ST/P004784/2). We are grateful to the staff at UKIRT and JCMT for their efforts in ensuring the success of the UDS project.

Appendix

A.1. Postage Stamp Images

In Figures 7 and 8, we show false-color thumbnail images with radio contours overlaid for the additional 6 GHz-selected

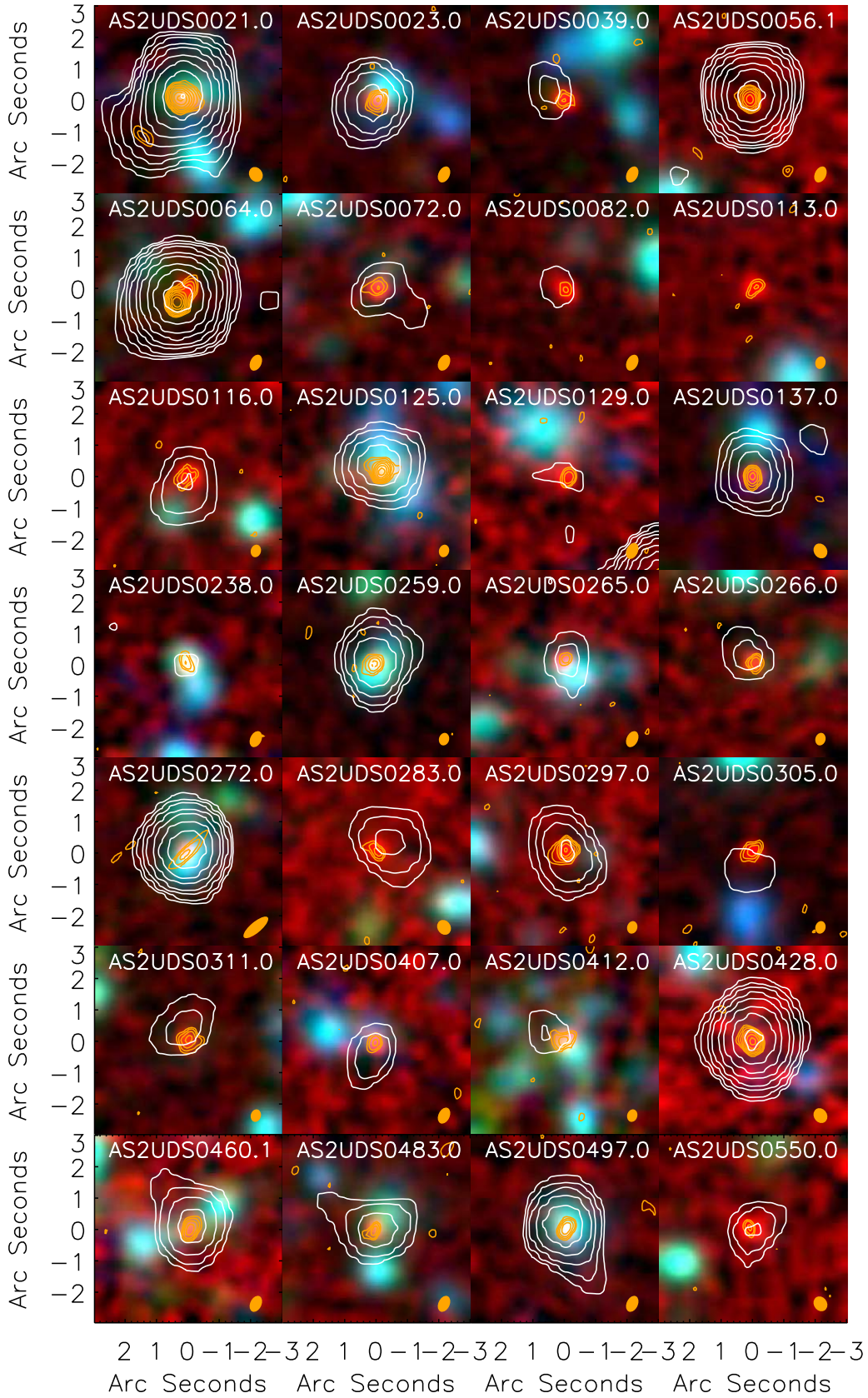


Figure 7. Thumbnail images of 28 SMGs with 5σ 6 GHz detections, highlighting the complex interplay between near-IR, dust, and radio continuum emission. False-color images and radio contours have the same meaning as in Figure 1. The 6 GHz PSF is shown as an orange ellipse in the bottom right of each panel.

SMGs not shown in Figure 1. False-color images comprise ALMA 870 μm (red), Subaru *i* (green), and V-band (blue), smoothed with a common $0''.35$ FWHM Gaussian. Radio

contours include 6 GHz (orange) and 1.4 GHz (white) overlaid at $-3, 3, 3\sqrt{2} \times \sigma$ (and in steps of $\sqrt{2} \times \sigma$ thereafter), highlighting the morphological diversity of our sources as a

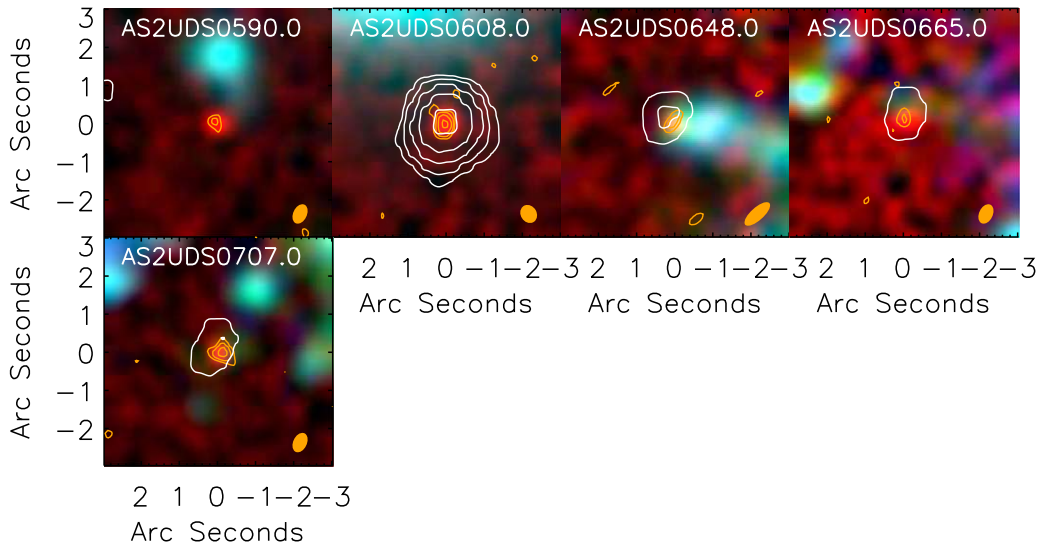


Figure 8. Thumbnail images of 5 SMGs with 5σ 6 GHz detections. False-color images and radio contours have the same meaning as in Figure 1. The 6 GHz PSF is shown as an orange ellipse in the bottom right of each panel.

function of wavelength. We show the VLA 6 GHz synthesized beam as an orange ellipse in the bottom right corner of each panel.

A.2. Flux Recovery and Deconvolved Size Estimates in High-resolution Radio Maps

We perform a series of tests in order to confirm the reliability of both the flux densities and sizes measured from our 6 GHz maps: first, we checked the absolute flux calibration of our reduced data by concatenating all scans of the phase calibrator source (J0215–0222) obtained under VLA project 15A-249, and making a multi-scale, multifrequency synthesis continuum image with natural weighting. The resolution of this image is $0''.52 \times 0''.37$ with a beam position angle $\theta = -41^\circ$, and we measured the flux density using the CASA IMFIT tool, recovering $S_{6\text{ GHz}} = 684 \pm 1\text{ mJy}$. This flux density is within $\sim 4\%$ of the canonical flux density quoted in the NRAO flux calibrator manual²⁴ ($S_{6\text{ GHz}} = 710\text{ mJy}$), indicating that the low target fluxes at 6 GHz are unlikely to be due to a systematic error in the absolute flux calibration of our data.

Next, we searched for signs that our naturally weighted, A-configuration 6 GHz observations may be insensitive to extended high-frequency emission by performing two independent tests. First, we re-imaged the data in WSCLEAN using the `-taper-gaussian lasec` option, which calculates and applies the required uv taper to degrade the image-plane resolution to $1''.0$, and created updated background and rms maps via boxcar smoothing. Tapering the uv data down weights the longer baselines and increases the beam area, trading off a (modest) loss in point-source sensitivity for an increase in sensitivity to extended emission. We performed blind source extraction on the tapered images using AEGERAN as described in Section 2, and then cross-checked the flux densities of sources detected in the tapered 6 GHz images with those of the naturally weighted maps. We detect only 21 SMGs in the tapered 6 GHz maps (compared to 41 SMGs in the untapered, naturally weighted maps), with good agreement in the flux densities for sources detected in both sets of maps (Figure 9). We therefore find little evidence

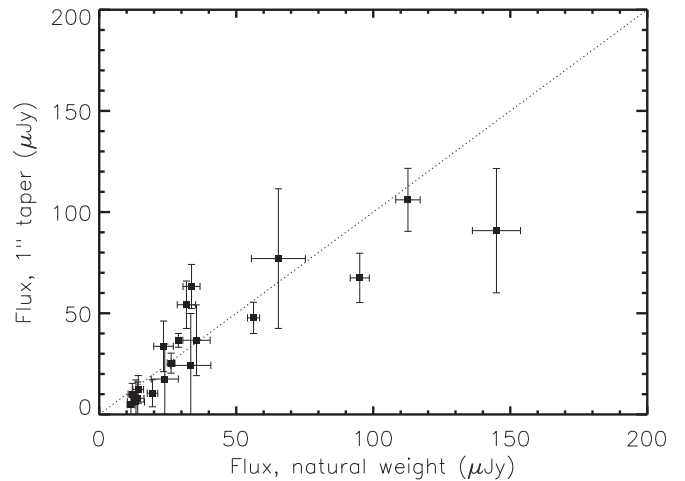


Figure 9. A comparison of the 6 GHz flux densities for 21 SMGs in the naturally weighted images used for analysis throughout this paper, with those measured in maps tapered to $1''$ resolution. If the spectral curvature seen in our 6 GHz-selected SMG sample were the result of having resolved-out flux on $\gtrsim 1''$ spatial scales, we would have expected to have recovered more flux in the tapered maps than in the naturally weighted maps. Instead, we find a good correspondence between the flux densities of SMGs detected in both sets of images, suggesting that our naturally weighted 6 GHz maps recover most of the flux in these systems, and that their low 6 GHz flux densities are unlikely to have been induced by the effects of uv coverage.

for any previously missed extended component on $\gtrsim 1''$ scales, suggesting that most of the 6 GHz flux is indeed located on the longer baselines, which trace compact $\sim 0''.5$ structures.

As an additional check (both against resolving out extended emission, and that our deconvolved source size estimates are probing real physical structures and are not merely the result of point sources that are broadened due to noise), we designed a suite of simulated 6 GHz data sets using the CASA task SIMOBSERVE, and then imaged, performed object detection, and measured deconvolved source sizes for these using the same workflow as was used for the real data (i.e., imaging the simulated data sets with WSCLEAN, performing object detection above a local 5σ threshold using AEGERAN, and then measuring

²⁴ <http://www.aoc.nrao.edu/~gtaylor/csource.html>

flux densities and deconvolved source sizes of detected sources with the CASA IMFIT task). These simulated observations were designed to have similar uv coverage to our real 6 GHz observations, i.e., using the VLA A-array antenna configuration file and with the simulated observations taking place in 2 hr intervals over a similar Local Sidereal Time (LST) range to the real observations. Realistic projection of our source models on to the VLA baselines was ensured via the World Coordinate System (WCS) information specified in the FITS header of the model image (i.e., using coordinates at the center of the UDS field). We construct two classes of model images.

A.2.1. Extended Source Models

The largest angular scale (θ_{LAS}) defines the largest scale structures to which an interferometer is sensitive, and can be determined theoretically from the fringe spacing formed by the shortest baseline in the array, $\theta_{\text{LAS}} \sim \lambda/B_{\text{min}}$. Emission from structures larger than θ_{LAS} forms fringes that destructively interfere (i.e., is “resolved out”). For 6 GHz observations undertaken with the VLA in A-configuration (where $B_{\text{min}} = 680$ m), we expect $\theta_{\text{LAS}} \sim 9''$ —thus for simulated observations obtained in this array/frequency combination we expect to be able to accurately recover the flux from extended sources and for this flux to be constant up to a source FWHM of at least several arcseconds, corresponding to $\gtrsim 60$ kpc at the median redshift of our sample ($z \sim 2.4$). This limiting physical extent is around $\sim 8\times$ larger than the typical optical half-light radii of SMGs (Swinbank et al. 2004; Chen et al. 2017), $\sim 10\times$ larger than their millimeter-wave dust continuum sizes (Simpson et al. 2015; Ikarashi et al. 2017), $\sim 4\times$ larger than their 1.4 GHz radio continuum sizes (Muxlow et al. 2005; Biggs & Ivison 2008; Jiménez-Andrade et al. 2019), and $4\times$ larger than their maximum reported cold ISM spatial extents (Carilli et al. 2011; Thomson et al. 2012; Riechers et al. 2013), and therefore offers an exceedingly generous upper limit on the scales to which our 6 GHz observations need to be sensitive.

To confirm the estimated $\sim 9''$ largest angular scale of the array and confirm our sensitivity to extended emission on the *relevant* range of spatial scales, we constructed a suite of 40 model images comprised of a single source (either a Gaussian or constant surface brightness disk model), placed at the phase center, with sizes (FWHM for the Gaussian model; diameter D for the disk model) between $0''$ and $15''$. These model images were used as the input models for 40 simulated observing runs, executed with the CASA SIMOBSERVE task. We use an integration interval of 10 s and a total observing time of 2 hr for each simulated observation in order to provide a close match for the uv coverage of our real 6 GHz observations. The resulting simulated measurement sets were then imaged with WSCLEAN, yielding a typical synthesized beam of $\sim 0''.48 \times 0''.40$ and a noise level $\sigma = 5 \mu\text{Jy beam}^{-1}$ with flux densities measured via aperture photometry for apertures $1.1\times$ the (known) extent of the input model. We find that for both Gaussian and constant surface brightness disk models, our chosen VLA array configuration is capable of recovering essentially all the flux of the input model for source sizes (FWHM and diameter, respectively) up to $\sim 6''.5$, and does not begin to significantly resolve out emission until the input source sizes are $\gtrsim 7''$. We show this drop-off in recovered flux as a function of input source size in Figure 10, which also includes symbols marking the typical dust continuum, 1.4 GHz and molecular gas sizes of SMGs at the same redshift. Our

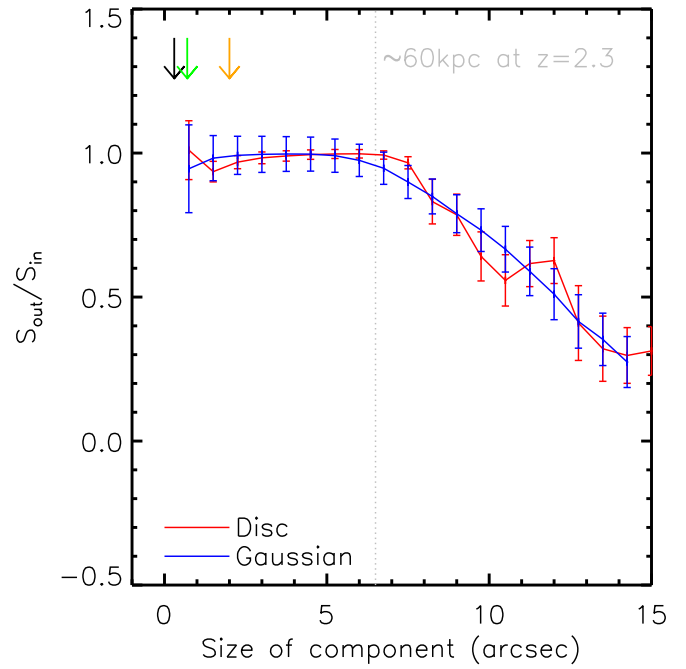


Figure 10. Ratio of recovered vs. input flux densities for simulated observations of model sources undertaken with the CASA SIMOBSERVE tool, with the array configuration, target declination, and LST range chosen to provide equivalent uv coverage to that of our 6 GHz VLA program. We see that for both Gaussian source models (with $0 < \text{FWHM} < 6''.5$) and constant surface brightness disk models (with diameter $0 < D < 7''$) the array can successfully recover $\sim 100\%$ of the input model flux, with a drop-off in sensitivity to flux on larger scales due to the lack of short spacings in the array. The angular scale at which this drop-off begins is very close to the theoretical largest angular scale of the array for sources observed at zenith in this array configuration ($\theta_{\text{LAS}} \sim \lambda/B_{\text{min}} \sim 9''$). We use colored arrows to highlight the typical angular sizes of SMGs measured in $870 \mu\text{m}$ dust continuum imaging with ALMA (~ 2 kpc; black arrow, Simpson et al. 2015), resolved 1.4 GHz *e*-MERLIN imaging (~ 5 kpc; green arrow, Biggs & Ivison 2008), and VLA observations of cold molecular gas ($^{12}\text{CO } J = 1-0$, ~ 16 kpc, orange arrow; Ivison et al. 2011). The empirical largest angular size of the VLA in A-Array for sources observed as the UDS field transits above Socorro is $\sim 6''.5$, corresponding to ~ 60 kpc at $z = 2.3$. Hence it is *highly* unlikely that the low observed 6 GHz continuum flux densities of our sources are the result of resolving out significant extended emission.

empirically derived largest angular scale is in excellent agreement with the expected θ_{LAS} , and is several times larger than the angular sizes of SMGs as seen in any other waveband. This strongly suggests that the lower-than-expected 6 GHz flux densities of our sources are not the result of resolving out extended flux.

A.2.2. Point-source Models

At modest S/N ($\lesssim 10$), image artifacts (including random noise, ripples, and other low-level calibration/data processing errors) may conspire to artificially broaden Gaussian fits to compact sources. To test the hypothesis that our deconvolved 6 GHz source sizes are simply the result of spurious broadening of unresolved sources due to noise (as opposed to real extended emission) we constructed a further five model images comprised of 2000 point sources each (initially distributed randomly within the model map, but with a check to remove any sources placed within $3''$ of any other source in order to sidestep issues associated with source blending), and with flux densities randomly distributed between 10 and $200 \mu\text{Jy}$. Again, these five model images served as the input models for five successive CASA SIMOBSERVE runs, which were again imaged

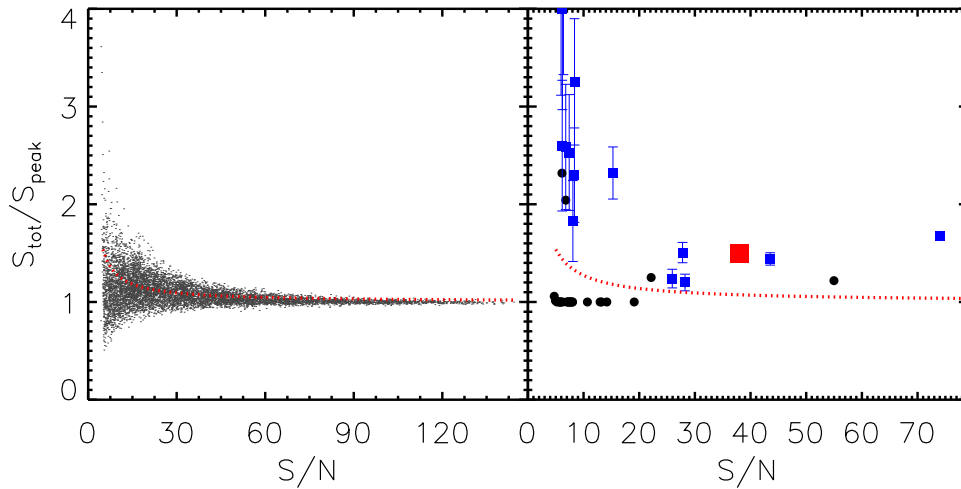


Figure 11. Left: ratio of integrated to peak flux densities measured by CASA IMFIT as a function of S/N for simulated VLA 6 GHz observations of $\sim 10,000$ point sources located in the UDS field. These simulated observations were executed using the CASA SIMOBSERVE task and were designed to produce similar uv coverage to our real 6 GHz observations (i.e., utilizing the VLA A-configuration antenna positions, and observing in 2 hr intervals over a comparable LST range), and were subjected to an identical imaging and cataloging workflow as was used for the real data (i.e., maps were made using WSCLEAN, which were cataloged with AEGEAN using a 5σ threshold for object detection before Gaussian components were fit to identified sources using the CASA IMFIT routine). To quantify the impact of spurious source broadening due to noise effects we measure the envelope (shown in red) below which $\sim 99\%$ of the sample lies as a function of S/N (see text for details), i.e., only $\sim 1\%$ of the point-source sample is scattered above this envelope by noise. Right: the ratio of total-to-peak flux density vs. S/N for the 41 6 GHz-detected SMGs in AS2UDS. Sources that are fit as point sources (or that are rejected as extended sources because $\theta/\delta\theta < 3$) are shown as open circles, while the 15 sources that have $\theta/\delta\theta \geq 3$ (and are thus classified as “resolved” by CASA IMFIT) are shown as blue squares. The convex-stacked subsample is represented with a large red square, and it, along with 15 individual SMGs lie above the empirically measured envelope, which highlights the domain of plausibly up-scattered sources. Hence, we classify them as being securely spatially resolved, and report their angular sizes in Table 1.

and cataloged following the same workflow as was used for the real 6 GHz maps.

To quantify the level of spurious source broadening it is helpful to plot the ratio of total-to-peak flux densities ($S_{\text{TOT}}/S_{\text{PEAK}}$) for recovered sources as a function of S/N for all 10,000 simulated point sources: for bona fide point sources, $S_{\text{TOT}}/S_{\text{PEAK}} \sim 1$, while $S_{\text{TOT}}/S_{\text{PEAK}} > 1$ highlights that the source-fitting procedure has determined that the source is spatially resolved. We show $S_{\text{TOT}}/S_{\text{PEAK}}$ versus S/N for our point-source models in Figure 11. To determine the reliability of source size estimates as a function of S/N we follow the examples of Bondi et al. (2008) and Smolčić et al. (2017) and empirically determine the envelope below which 99% of the simulated data points lie in bins of S/N. We fit a curve of the form $S_{\text{TOT}}/S_{\text{PEAK}} = 1 + A(S/N)^B$ to this envelope, finding that the coefficients $A = 2.7$ and $B = -9.8$ provide a good fit; only 1% of our simulated point sources suffer from severe-enough spurious broadening to be elevated above this line, and therefore we use this empirical envelope to provide further quality assurance on the deconvolved 6 GHz source sizes reported in Section 3.4. Of the seventeen 6 GHz-detected SMGs that are reported as “resolved” by CASA IMFIT (i.e., satisfying the criteria that $S/N \geq 5$ and $\theta/\delta\theta \geq 3$), we find that two (AS2UDS 003.0 and 407.0) lie below this source-broadening envelope. We therefore conservatively reclassify these sources as being unresolved 6 GHz detections. The remaining 15 SMGs—and the stacked subsamples—all lie comfortably above this envelope, and are hence considered to be resolved sources.

A.2.3. The Uncertainties on Deconvolved Source Sizes

Finally, and returning to our real 6 GHz data, we conduct an assessment of the reliability of the algorithm used by CASA IMFIT to compute deconvolved source sizes (θ) and their uncertainties ($\delta\theta$) from their fitted (i.e., image-based) size and uncertainty (ϕ and $\delta\phi$, respectively).

In an important work, Condon (1997) outlines the formalism for determining errors in elliptical Gaussian fits. Using Equation (21) of Condon (1997), we see that a source with a fitted axis size ϕ has an uncertainty σ_ϕ on that fitted size of

$$\left(\frac{\sigma_\phi}{\phi}\right)^2 \approx \frac{2}{\rho^2}, \quad (11)$$

where in Equation (41) of the same work it is shown that

$$\rho^2 = \frac{\phi_M \phi_m}{4\phi_N^2} \left[1 + \left(\frac{\phi_N}{\phi_M}\right)^2 \right]^{\alpha_M} \left[1 + \left(\frac{\phi_N}{\phi_m}\right)^2 \right]^{\alpha_m} \frac{S_{\text{peak}}^2}{\sigma_{\text{peak}}^2} \quad (12)$$

is the overall S/N of the Gaussian fit. Here, ϕ_M and ϕ_m are the fitted major/minor axis sizes, respectively, ϕ_N is the angular scale (FWHM) on which the image noise is correlated, i.e., approximately the synthesized beam size. The exponents α_M/α_m were empirically derived by Condon (1997) for a variety of source models, with $\alpha_M \sim 5/2$ and $\alpha_m \sim 1/2$ being found for source sizes close to the telescope synthesized beam. $S_{\text{peak}}/\sigma_{\text{peak}} \equiv \text{SNR}$ is the ratio of the peak amplitude of the Gaussian fit to the local rms.

We compute uncertainties on the fitted major/minor axis sizes of our 6 GHz resolved SMG sample using these relations, finding them to be in good agreement with the fitted size errors reported by CASA IMFIT. Next, we propagate these uncertainties on the fitted source sizes through to the *deconvolved* source sizes (i.e., the intrinsic sizes of our sources after deconvolving the telescope PSF) using Equations (2) and (3) of Murphy et al. (2017):

$$\theta = \sqrt{\phi^2 - \theta_{1/2}^2} \quad (13)$$

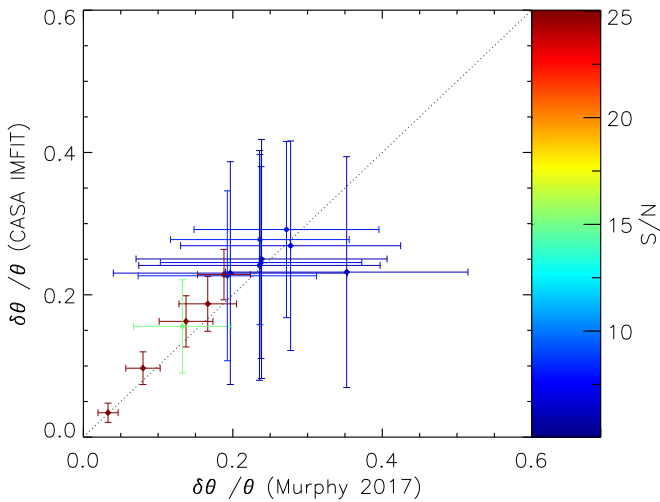


Figure 12. Comparison of the 6 GHz fractional deconvolved source size error estimates (i.e., $\delta\theta/\theta$, where θ is the deconvolved source size and $\delta\theta$ is the error on this value) determined by the CASA IMFIT routine vs. those calculated from the fitted (i.e., non-deconvolved) source sizes/errors using the relations of Condon (1997) and Murphy et al. (2017) for the 15 SMGs with measured 6 GHz sizes in Table 1. Points are color-coded by the peak S/N, and the error bars show the fractional uncertainty in the peak fluxes (i.e., N/S). We see excellent agreement between the deconvolved source size estimates measured by CASA IMFIT and those computed using the Condon (1997) and Murphy et al. (2017) relations across our sample, within the error bars set by the S/N of the data, suggesting that the deconvolved source size uncertainties reported by CASA are reliable at least down to the 5σ flux cut used for source-finding in Section 2.

$$\left(\frac{\delta\theta}{\delta\phi}\right) = \left[1 - \left(\frac{\theta_{1/2}}{\phi}\right)^2\right]^{-1/2}, \quad (14)$$

where $\theta_{1/2}$ is the fitted beam size.

Specifically, we are interested in the fractional error on the deconvolved source sizes, $\delta\theta/\theta$, and in studying how this evolves with S/N. In general, we would expect sources detected at lower S/N to have higher fractional uncertainties on their deconvolved sizes, however any systematic errors with the way in which CASA IMFIT propagates the uncertainty on the fitted size through to the uncertainty on the deconvolved source size might be expected to produce a second-order effect that correlates with the S/N of the observation. We return to the CASA IMFIT outputs for the 15 SMGs we formally classify as “resolved” (Table 1) and compare $\delta\theta_{\text{CASA}}$ with $\delta\theta_{\text{Murphy,2017}}$ (which we compute from the fitted size uncertainties calculated above) in Figure 12. We see excellent agreement between the deconvolved source sizes (and their uncertainties) returned automatically by the CASA IMFIT source fitter and those calculated from the (non-deconvolved) Gaussian fits using the relations of Condon (1997) and Murphy et al. (2017).

Hence, our 6 GHz source size estimates are most likely not the result of spurious broadening of unresolved emission due to image-plane noise and/or due to errors in the fitting procedure used in CASA IMFIT.

A.3. A Note on Possible Free–Free Suppression

In a recent study on the radio spectral properties of the nuclear disks of Arp 220, Barcos-Muñoz et al. (2015) observed a remarkably consistent spectral index $\alpha \sim -0.7$ in four frequency ranges between 4.7 and 43.5 GHz. Hence, the Arp 220 radio SED neither steepens toward higher frequencies

(as happens in our SMG sample) nor flattens toward higher frequency due to free–free emission (as is seen in local, “normal” star-forming galaxies). Barcos-Muñoz et al. (2015) argue that both this SED shape, and the high brightness temperatures ($\sim 10^4$ K at 6 GHz) of Arp 220 indicate a radio SED that is dominated at all frequencies by nonthermal synchrotron emission, with no (or little) need for any additional contribution arising from a flatter spectrum, thermal free–free component. While the high SFRs ($\text{SFR} \sim 200 M_\odot \text{ yr}^{-1}$) in the disks of Arp 220 suggest that a strong free–free component *should* be present, Barcos-Muñoz et al. (2015) argue that in sufficiently dusty environments, a non-negligible fraction of ultraviolet photons can be absorbed *before* they produce the ionizations that are a prerequisite for thermal radio emission, thus lowering the thermal luminosity density relative to that expected, given the SFR.

The high dust masses of SMGs ($M_{\text{dust}} \geq 10^8 M_\odot$; e.g., Santini et al. 2010; Swinbank et al. 2014) and their large optical extinctions ($A_V \geq 500$; e.g., Simpson et al. 2017) certainly suggest that if such suppression of thermal emission is indeed possible, then SMGs represent an environment in which this phenomenon could be important.²⁵

To test whether the conclusions of our model for synchrotron spectral aging are sensitive to the assumed strength of the free–free component, we reran the model for $t_{\text{sync}} = 0\text{--}200$ Myr and $B = 1\text{--}100 \mu\text{G}$ under the extreme assumption that the free–free component is completely suppressed—that is, requiring that the aged-synchrotron models fit the observed composite SED directly, with no prior subtraction of a scaled $\alpha \sim -0.1$ power-law contribution (Figure 5). We find that suppressing the thermal component in this manner allows for synchrotron ages that are $\sim 5\text{--}15$ Myr lower (for a given magnetic field strength) than are obtained from models in which the thermal component scales with the far-IR derived SFR, SFR_{IR} , but that the interpretation of our models is not fundamentally changed. We show examples SEDs for the synchrotron fits without free–free emission in Figure 5.


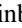


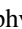



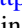






A.4. AS2UDS0017.1: A Radio-bright, Gas-rich, 870 μm -faint Galaxy at $z \sim 2.6$

The 6 GHz thumbnail of one of our sources (AS2UDS0017.1; previously published under the ID UDS 306.1 by Simpson et al. 2015; Wardlow et al. 2018) shows an extension/secondary component located $\sim 1''$ (~ 8 kpc) from the peak of the 870 μm detection. This 6 GHz emission has no 870 μm continuum counterpart, but has a resolved optical/near-IR counterpart whose color is similar to that of the SMG, as well as a confirmed $^{12}\text{CO } J=3\text{--}2$ detection at the same redshift as the SMG (Wardlow et al. 2018). While radio jets have been found to be capable both of driving outflows of molecular gas from an AGN host (e.g., Dasyra et al. 2015), and of triggering star formation where they

²⁵ Alternatively, if the IMF is top heavy—a claim first made by Baugh et al. (2005), as a necessary condition for matching observed and theoretical number counts of starburst galaxies, but recently lent its first direct observational support in the form of CNO isotope yields in starburst galaxies that are consistent with enhanced production of AGB stars (Romano et al. 2017)—then the resulting enhancement of L_{IR} per unit SFR would imply up to a factor $\sim 4\times$ enhancement in the L_{IR}/SFR ratio compared to that used in Kennicutt (1998), which assumed a Salpeter (1955) IMF. Such an enhancement in the L_{IR}/SFR ratio would naturally lead to an over-prediction of the free–free luminosity density if inferred from L_{IR} without taking the top-heavy nature of the IMF into account.

collide with the ISM of nearby galaxies (e.g., Lacy et al. 2017), the coexistence of strong radio and molecular gas emission, along with a bright optical counterpart that is clearly distinct from the SMG suggests that this radio feature is unlikely to be a jet originating in AS2UDS0017.1, but is instead a separate star-forming companion galaxy at the same redshift. A detailed analysis of this source is presented in Wardlow et al. (2018), however for the present work, we note the complex radio morphology, and fit the 6 GHz thumbnail with two Gaussian components. The source size quoted in Table 1 is that of the component aligned with the 870 μm emission only.

ORCID iDs

Ian Smail  <https://orcid.org/0000-0003-3037-257X>
 A. M. Swinbank  <https://orcid.org/0000-0003-1192-5837>
 J. M. Simpson  <https://orcid.org/0000-0002-8521-1995>
 S. Stach  <https://orcid.org/0000-0003-1122-6948>
 E. J. Murphy  <https://orcid.org/0000-0001-7089-7325>
 W. Rujopakarn  <https://orcid.org/0000-0002-0303-499X>
 O. Almaini  <https://orcid.org/0000-0001-9328-3991>
 F. An  <https://orcid.org/0000-0001-7943-0166>
 A. W. Blain  <https://orcid.org/0000-0001-7489-5167>
 C. C. Chen  <https://orcid.org/0000-0002-3805-0789>
 E. A. Cooke  <https://orcid.org/0000-0003-3843-8393>
 A. C. Edge  <https://orcid.org/0000-0002-3398-6916>
 D. Farrah  <https://orcid.org/0000-0003-1748-2010>
 P. van der Werf  <https://orcid.org/0000-0001-5434-5942>
 J. L. Wardlow  <https://orcid.org/0000-0003-2376-8971>

References

- Aguirre, P., Baker, A. J., Menanteau, F., Lutz, D., & Tacconi, L. J. 2013, *ApJ*, **768**, 164
- Banerji, M., Chapman, S. C., Smail, I., et al. 2011, *MNRAS*, **418**, 1071
- Barcos-Muñoz, L., Leroy, A. K., Evans, A. S., et al. 2015, *ApJ*, **799**, 10
- Basu, A., Beck, R., Schmidt, P., & Roy, S. 2015, *MNRAS*, **449**, 3879
- Baugh, C. M., Lacey, C. G., Frenk, C. S., et al. 2005, *MNRAS*, **356**, 1191
- Biggs, A. D., & Ivison, R. J. 2008, *MNRAS*, **385**, 893
- Bisbas, T. G., van Dishoeck, E. F., Papadopoulos, P. P., et al. 2017, *ApJ*, **839**, 90
- Bondi, M., Cilieggi, P., Schinnerer, E., et al. 2008, *ApJ*, **681**, 1129
- Bothwell, M. S., Smail, I., Chapman, S. C., et al. 2013, *MNRAS*, **429**, 3047
- Bourne, N., Dunne, L., Ivison, R. J., et al. 2011, *MNRAS*, **410**, 1155
- Brisbin, D., Miettinen, O., Aravena, M., et al. 2017, *A&A*, **608**, A15
- Bruzual, G., & Charlot, S. 2003, *MNRAS*, **344**, 1000
- Calistro Rivera, G., Williams, W. L., Hardcastle, M. J., et al. 2017, *MNRAS*, **469**, 3468
- Carilli, C. L., & Barthel, P. D. 1996, *A&ARv*, **7**, 1
- Carilli, C. L., Hodge, J., Walter, F., et al. 2011, *ApJL*, **739**, L33
- Chabrier, G. 2003, *PASP*, **115**, 763
- Chapman, S. C., Blain, A. W., Smail, I., & Ivison, R. J. 2005, *ApJ*, **622**, 772
- Charlot, S., & Fall, S. M. 2000, *ApJ*, **539**, 718
- Chen, C.-C., Hodge, J. A., Smail, I., et al. 2017, *ApJ*, **846**, 108
- Chen, C.-C., Smail, I., Swinbank, A. M., et al. 2015, *ApJ*, **799**, 194
- Condon, J. J. 1992, *ARA&A*, **30**, 575
- Condon, J. J. 1997, *PASP*, **109**, 166
- da Cunha, E., Charlot, S., & Elbaz, D. 2008, *MNRAS*, **388**, 1595
- da Cunha, E., Walter, F., Smail, I., et al. 2015, *ApJ*, **806**, 110
- Dahlem, M., Lisenfeld, U., & Golla, G. 1995, *ApJ*, **444**, 119
- Danielson, A. L. R., Swinbank, A. M., Smail, I., et al. 2017, *ApJ*, **840**, 78
- Dannerbauer, H., Lehnert, M. D., Emonts, B., et al. 2017, *A&A*, **608**, A48
- Dasyra, K. M., Bostrom, A. C., Combes, F., & Vlahakis, N. 2015, *ApJ*, **815**, 34
- Del Moro, A., Alexander, D. M., Mullaney, J. R., et al. 2013, *A&A*, **549**, A59
- Delhaize, J., Smolčić, V., Delvecchio, I., et al. 2017, *A&A*, **602**, A4
- Donley, J. L., Koekemoer, A. M., Brusa, M., et al. 2012, *ApJ*, **748**, 142
- Dunne, L., Ivison, R. J., Maddox, S., et al. 2009, *MNRAS*, **394**, 3
- Emonts, B. H. C., Lehnert, M. D., Villar-Martín, M., et al. 2016, *Sci*, **354**, 1128
- Galvin, T. J., Seymour, N., Marvil, J., et al. 2018, *MNRAS*, **474**, 779
- Garrett, M. A. 2002, *A&A*, **384**, L19
- Geach, J. E., Dunlop, J. S., Halpern, M., et al. 2017, *MNRAS*, **465**, 1789
- George, R. D., Ivison, R. J., Smail, I., et al. 2014, *MNRAS*, **442**, 1877
- Grenier, I. A., Black, J. H., & Strong, A. W. 2015, *ARA&A*, **53**, 199
- Gullberg, B., Swinbank, A. M., Smail, I., et al. 2018, *ApJ*, **859**, 12
- Hancock, P. J., Murphy, T., Gaensler, B. M., Hopkins, A., & Curran, J. R. 2012, *Aegean: Compact Source Finding in Radio Images*. Astrophysics Source Code Library, ascl:1212.009
- Heesen, V., Beck, R., Krause, M., & Dettmar, R.-J. 2009, *A&A*, **494**, 563
- Heesen, V., Dettmar, R.-J., Krause, M., Beck, R., & Stein, Y. 2016, *MNRAS*, **458**, 332
- Helou, G., Soifer, B. T., & Rowan-Robinson, M. 1985, *ApJL*, **298**, L7
- Hickox, R. C., Wardlow, J. L., Smail, I., et al. 2012, *MNRAS*, **421**, 284
- Hodge, J. A., Karim, A., Smail, I., et al. 2013, *ApJ*, **768**, 91
- Hodge, J. A., Swinbank, A. M., Simpson, J. M., et al. 2016, *ApJ*, **833**, 103
- Hughes, D. H., Serjeant, S., Dunlop, J., et al. 1998, *Natur*, **394**, 241
- Hunt, L. K., & Maiolino, R. 2005, *ApJL*, **626**, L15
- Ibar, E. 2009, PhD thesis, Univ. Edinburgh, <https://www.era.lib.ed.ac.uk/handle/1842/3845>
- Ibar, E., Ivison, R. J., Best, P. N., et al. 2010, *MNRAS*, **401**, L53
- Ikarashi, S., Ivison, R. J., Caputi, K. I., et al. 2017, *ApJ*, **835**, 286
- Ivison, R. J., Chapman, S. C., Faber, S. M., et al. 2007, *ApJL*, **660**, L77
- Ivison, R. J., Greve, T. R., Smail, I., et al. 2002, *MNRAS*, **337**, 1
- Ivison, R. J., Magnelli, B., Ibar, E., et al. 2010, *A&A*, **518**, L31
- Ivison, R. J., Papadopoulos, P. P., Smail, I., et al. 2011, *MNRAS*, **412**, 1913
- Ivison, R. J., Smail, I., Le Borgne, J.-F., et al. 1998, *MNRAS*, **298**, 583
- Jiménez-Andrade, E. F., Magnelli, B., Karim, A., et al. 2019, *A&A*, **625**, A114
- Kardashev, N. S. 1962, *SvA*, **6**, 317
- Kennicutt, R. C., Jr. 1998, *ApJ*, **498**, 541
- Kocevski, D. D., Hasinger, G., Brightman, M., et al. 2018, *ApJS*, **236**, 48
- Lacki, B. C., & Thompson, T. A. 2010, *ApJ*, **717**, 196
- Lacy, M., Croft, S., Fragile, C., Wood, S., & Nyland, K. 2017, *ApJ*, **838**, 146
- Lindroos, L., Knudsen, K. K., Vlemmings, W., Conway, J., & Martí-Vidal, I. 2015, *MNRAS*, **446**, 3502
- Lisenfeld, U., Voelk, H. J., & Xu, C. 1996, *A&A*, **314**, 745
- Magnelli, B., Ivison, R. J., Lutz, D., et al. 2015, *A&A*, **573**, A45
- McMullin, J. P., Waters, B., Schiebel, D., Young, W., & Golap, K. 2007, in *ASP Conf. Ser. 376, Astronomical Data Analysis Software and Systems XVI*, ed. R. A. Shaw, F. Hill, & D. J. Bell (San Francisco, CA: ASP), **127**
- Meijerink, R., Spaans, M., Loenen, A. F., & van der Werf, P. P. 2011, *A&A*, **525**, A119
- Miettinen, O., Novak, M., Smolčić, V., et al. 2017, *A&A*, **602**, A54
- Mulcahy, D. D., Horneffer, A., Beck, R., et al. 2018, *A&A*, **615**, A98
- Murphy, E. J. 2009, *ApJ*, **706**, 482
- Murphy, E. J., Helou, G., Kenney, J. D. P., Armus, L., & Braun, R. 2008, *ApJ*, **678**, 828
- Murphy, E. J., Helou, G., Kenney, J. D. P., Armus, L., & Braun, R. 2011, *ApJ*, **737**, 67
- Murphy, E. J., Momjian, E., Condon, J. J., et al. 2017, *ApJ*, **839**, 35
- Muxlow, T. W. B., Richards, A. M. S., Garrington, S. T., et al. 2005, *MNRAS*, **358**, 1159
- Nath, B. B., Gupta, N., & Biermann, P. L. 2012, *MNRAS*, **425**, L86
- Offringa, A. R., McKinley, B., Hurley-Walker, N., et al. 2014, *MNRAS*, **444**, 606
- Offringa, A. R., van de Gronde, J. J., & Roerdink, J. B. T. M. 2012, *A&A*, **539**, A95
- Pacholczyk, A. G. 1970, *Radio Astrophysics. Nonthermal Processes in Galactic and Extragalactic Sources* (San Francisco, CA: Freeman)
- Papadopoulos, P. P., Thi, W.-F., Miniati, F., & Viti, S. 2011, *MNRAS*, **414**, 1705
- Radcliffe, J. F., Beswick, R. J., Thomson, A. P., et al. 2019, *MNRAS*, in press (arXiv:1909.12588)
- Riechers, D. A., Bradford, C. M., Clements, D. L., et al. 2013, *Natur*, **496**, 329
- Riechers, D. A., Carilli, C. L., Capak, P. L., et al. 2014, *ApJ*, **796**, 84
- Romano, D., Matteucci, F., Zhang, Z.-Y., Papadopoulos, P. P., & Ivison, R. J. 2017, *MNRAS*, **470**, 401
- Salpeter, E. E. 1955, *ApJ*, **121**, 161
- Santini, P., Maiolino, R., Magnelli, B., et al. 2010, *A&A*, **518**, L154
- Schleicher, D. R. G., & Beck, R. 2013, *A&A*, **556**, A142
- Schleicher, D. R. G., & Beck, R. 2016, *A&A*, **593**, A77
- Simpson, J. M., Smail, I., Swinbank, A. M., et al. 2015, *ApJ*, **799**, 81
- Simpson, J. M., Smail, I., Swinbank, A. M., et al. 2017, *ApJ*, **839**, 58
- Simpson, J. M., Swinbank, A. M., Smail, I., et al. 2014, *ApJ*, **788**, 125
- Smail, I., Ivison, R. J., & Blain, A. W. 1997, *ApJL*, **490**, L5
- Smith, H. E., Lonsdale, C. J., Lonsdale, C. J., & Diamond, P. J. 1998, *ApJL*, **493**, L17

- Smolčić, V., Novak, M., Bondi, M., et al. 2017, [A&A](#), **602**, A1
- Stach, S. M., Dudzevičiūtė, U., Smail, I., et al. 2019, [MNRAS](#), **487**, 4648
- Strong, A. W., & Moskalenko, I. V. 1998, [ApJ](#), **509**, 212
- Strong, A. W., Moskalenko, I. V., & Ptuskin, V. S. 2007, [ARNPS](#), **57**, 285
- Swinbank, A. M., Smail, I., Chapman, S. C., et al. 2004, [ApJ](#), **617**, 64
- Swinbank, A. M., Simpson, J. M., Smail, I., et al. 2014, [MNRAS](#), **438**, 1267
- Tatischeff, V., & Kiener, J. 2004, [NewAR](#), **48**, 99
- Thompson, T. A., Quataert, E., Waxman, E., Murray, N., & Martin, C. L. 2006, [ApJ](#), **645**, 186
- Thomson, A. P., Ivison, R. J., Simpson, J. M., et al. 2014, [MNRAS](#), **442**, 577
- Thomson, A. P., Ivison, R. J., Smail, I., et al. 2012, [MNRAS](#), **425**, 2203
- Thomson, A. P., Muxlow, T. W. B., Smail, I., et al. 2019, [arXiv:1902.02356](#)
- Thomson, A. P., Simpson, J. M., Smail, I., et al. 2017, [ApJ](#), **838**, 119
- Tisanić, K., Smolčić, V., Delhaize, J., et al. 2019, [A&A](#), **621**, A139
- Toft, S., Smolčić, V., Magnelli, B., et al. 2014, [ApJ](#), **782**, 68
- Ueda, Y., Watson, M. G., Stewart, I. M., et al. 2008, [ApJS](#), **179**, 124
- Uhlig, M., Pfrommer, C., Sharma, M., et al. 2012, [MNRAS](#), **423**, 2374
- Wardlow, J. L., Simpson, J. M., Smail, I., et al. 2018, [MNRAS](#), **479**, 3879
- Wilkinson, A., Almaini, O., Chen, C.-C., et al. 2017, [MNRAS](#), **464**, 1380
- Yun, M. S., Scott, K. S., Guo, Y., et al. 2012, [MNRAS](#), **420**, 957
- Zweibel, E. 2013, [Natur](#), **502**, 453